

Total Lagrangian Smoothed Particle Hydrodynamics with An Improved Bond-Based Deformation Gradient for Large Strain Solid Dynamics

I. M. Wiragunarsa^a, L. R. Zuhail^{a,*}, T. Dirgantara^a, I. S. Putra^a, E. Febrianto^{a,b}

^a*Faculty of Mechanical and Aerospace Engineering, Institut Teknologi Bandung, Ganesa Street 10, Bandung, 40132, Indonesia*

^b*Glasgow Computational Engineering Centre, University of Glasgow, University Avenue, Glasgow, G12 8QQ, UK*

Abstract

Total Lagrangian Smoothed Particle Hydrodynamics (TLSPH) is one variant of SPH where the variables are described using the fixed reference configuration and a Lagrangian smoothing kernel. TLSPH elevates the computational efficiency of the standard SPH when no topological change is involved, and it alleviates the stability of SPH scheme with respect to tensile loading. However, instabilities associated with spurious mode, or hourglass/zero-energy mode, persists and often affects the simulation of solids undergoing extremely large strain. This work proposes an alternative formulation to compute deformation gradient with improved accuracy and therefore minimising the possibility of encountering the zero-energy mode. Specifically, we leverage the local discrete computation of bond-based (or pairwise) deformation gradient smoothed by the kernel. Additionally, the bond of a particle with itself is considered to preserve the polynomial reproducibility imposed by the kernel correction scheme. We showcase the convergence of the approach using a two-dimensional benchmark example. Furthermore, the accuracy, robustness, and stability of the proposed approach are assessed in various two- and three-dimensional examples, highlighting on the stability improvement that allows for solid dynamic simulations with more extreme elongation.

Keywords: SPH, Particle Methods, Computational Solid Mechanics

1. Introduction

Smoothed particle hydrodynamics (SPH) is a meshfree method that uses kernel estimates to approximate a continuous field over the domain [1–3]. In SPH, the continuum is discretised using a finite set of particles, where the discrete values of the fields are sampled. The continuous field is then obtained by accounting the contribution of the neighbouring particles weighted by the kernel. Owing to its meshfree nature, SPH avoids challenges in creating analysis-suitable meshes commonly found in the mesh-based computational methods [4, 5]. Over the years, SPH has been applied to various scientific and engineering problems, including linear and nonlinear solid mechanics [6], structural dynamics [7], crack propagations [8, 9], and problems involving high distortion and impact [10–13]. Despite its notable success, SPH is not without its challenges, manifesting in issues such as lack of consistency, tensile instability, and the presence of zero-energy or hourglass mode [14, 15].

The consistency issue in SPH is often attributed to the discrete approximation of the convolution integral, which prohibits the scheme to reproduce polynomial of order p . This limitation becomes more pronounced when the particle distribution is non-uniform, and in the region near the boundaries. To address this challenge, a common strategy in SPH involves introducing corrections to the kernel, ensuring the reproducibility of polynomials up to a certain order [16, 17]. This approach is also employed in other meshless methods [18]. When the governing equation involves only the first derivative, the correction can be applied to the gradient rather than the kernel itself [19, 20]. In certain cases, this modification proves to be more computationally efficient and is adequate for achieving linear consistency.

*Corresponding author

Email address: lavi.zuhail@itb.ac.id (L. R. Zuhail)

However, one drawback of the correction approach is the loss of symmetry in the kernel, and similarly, its gradient is no longer anti-symmetric, impacting the local momentum and energy preservation. To reconcile both consistency and local conservation, one potential solution is to symmetrise the kernel and its gradient, as demonstrated for instance in [21].

There are two known sources of instability in the classical, or updated Lagrangian, SPH (ULSPH) formulation. The first is instability under tensile loading, and the second is associated with the zero-energy or hourglass mode. Comprehensive stability analyses of ULSPH are presented in [22, 23]. Various approaches have been proposed to address the issue of tensile instability, including the introduction of artificial viscosity [24, 25] and artificial stress [26], conservative smoothing [27–30], a stable adaptive kernel [31], and the addition of a separate set of points to evaluate derivatives, known as stress points [32]. Despite being the most prevalent in SPH, the artificial viscosity may lead to an excessive dissipation [33]. When SPH is formulated with a Lagrangian kernel, the issue of tensile instability can be eliminated without introducing additional terms to the governing equation. This is often referred to as total Lagrangian SPH (TLSPH) [34–36]. Furthermore, in TLSPH, the field variables are described in the reference configuration, resulting in a computationally efficient scheme as the neighbour search is performed only once. In recent years, TLSPH has found successful applications in various aspects of solid mechanics, including those involving geometric nonlinearity [37–39], solid dynamics [40, 41], and simulations of crack growth [42].

While TLSPH effectively resolves the issue of tensile instability, the persistent presence of oscillation due to the zero-energy, or hourglass, modes remains a challenge. The zero-energy mode is observed in various other numerical methods, including finite difference and finite elements [43, 44], and is attributed to the inaccuracies in estimating the gradient of a discretely represented field. Numerous methods have been proposed to address the zero-energy mode, such as δ -SPH diffusive terms [45–47], the Rieman solver [48], and moving least square stress regularisation [49, 50]. The most notable treatment for hourglass instability is the stress-point approach [51, 52], which determines the field gradient on a separate set of nodes, sharing roots with the staggered grid approach in finite difference [53–55]. In the context of TLSPH, a notable approach involves adding a correctional force [56], analogous to those proposed in finite elements. A recent work by Wu [57] introduces a non-hourglass TLSPH formulation that decomposes the shear deformation and stress according to the volumetric and deviatoric contributions. Despite showing a significant stability improvement with respect to the hourglass mode, both approaches rely on a set of user-prescribed parameters that are problem dependent, which requires thorough parametric studies.

This work proposes an alternative approach to improve the stability of the TLSPH scheme, specifically targeting the spurious zero-energy mode, without depending on user-defined parameters. Our key ingredient is the alternative expression to compute the deformation gradient, which utilises local pair-wise discrete gradient estimates weighted by the Lagrangian kernel. It is noteworthy that the conventional TLSPH approach in computing the deformation gradient involves smoothing the discrete deformation weighted by the gradient of the Lagrangian kernel. Our proposed methodology traces back to the differentiation identity of the convolution of continuous functions, i.e., $D(W * x) = D W * x = W * D x$. A similar concept has also been proposed in peridynamics [58, 59], which is referred to as bond-based deformation gradient approach. In contrast to this approach, we include in our proposal an estimate for the deformation gradient at the particle, leveraging the standard gradient estimate in TLSPH. We demonstrate through a simple one-dimensional example that our proposal improves the gradient estimation and preserves the polynomial reproducibility of the scheme, as governed by the corrected kernel. We tailor our proposed deformation gradient estimate in a mixed formulation TLSPH following the framework of [60–62], enhancing it with the Jameson-Schmidt-Turkel (JST) scheme to prevent excessive dissipation in dynamic simulations. Additionally, for time integration, we employ an explicit three-stage time integrator [63], enabling the use of higher CFL numbers and resulting in faster computational times with second-order accuracy [64]. Furthermore, we validate the proposed approach through various benchmark cases in 2D and 3D, showcasing improved accuracy and stability.

The structure of this paper is as follows. First, we revisit the spatial discretisation in SPH including the kernel correction necessary for achieving the desired polynomial reproducibility. Subsequently, we discuss the total Lagrangian SPH formulation by deriving from the conservation laws and employing the spatial discretisation based on the corrected Lagrangian kernel. In the next section we describe the proposed alternative estimation of the deformation gradient. We provide an illustration of the proposed approach in one-dimensional setting and subsequently detail its integration into our TLSPH framework. Next we present several numerical examples in two and three dimensions, within the context of solid dynamic problems. In the concluding section, we summarise our study on the proposed approach and outline potential future works.

2. Spatial discretisation in SPH

In this section, we discuss the spatial discretisation in SPH by considering a scalar field $f(\mathbf{x})$, where $\mathbf{x} \in \Omega$ represents spatial coordinates in \mathbb{R}^d , with $d \in \{1, 2, 3\}$. In this context, we assume that the domain Ω remains static and undeformed, eliminating the need to distinguish between the current and reference systems. The discretisation of the field involves employing values obtained at a finite point set, referred to as particles. The relationship between the discrete point-wise values and the continuous form $f(\mathbf{x})$ is established through the SPH discretisation, utilising a kernel with finite support. This section further details the treatments necessary to ensure compliance with the linear polynomial reproducibility conditions.

2.1. Field approximation from point values

We start our discussion with the acquisition of a smooth approximation for an arbitrary field $f(\mathbf{x})$ through convolutional smoothing with a kernel $W(\mathbf{x})$

$$\widehat{f}(\mathbf{x}) = \int_{\Omega} f(\mathbf{x}') W(\mathbf{x} - \mathbf{x}', h) d\mathbf{x}'. \quad (1)$$

The smoothing kernel is typically required to be positive, has a unit volume, and be compactly supported [5]. When choosing kernels with compact support, the integration domain in (1) can be simplified from the whole domain Ω to only the kernel support centred at evaluation point \mathbf{x} . In this work, we focus on radial kernels with a compact support of radius $R = \kappa h$, where h represents the characteristic smoothing length of the kernel. The factor κ varies based on the type of kernel used, for example, $\kappa = 2$ for cubic spline and $\kappa = 3$ for quintic spline kernel [5]. It is noteworthy that as h approaches 0, the kernel W becomes a Dirac's delta function $\delta(\mathbf{x} - \mathbf{x}')$. The application of $\delta(\mathbf{x} - \mathbf{x}')$ as a kernel in (1) yields the identity $\widehat{f}(\mathbf{x}) = f(\mathbf{x})$. However, in general this identity does not hold for arbitrary kernels, and the approximation $\widehat{f}(\mathbf{x})$ deviates from the original function $f(\mathbf{x})$ according to the moments of the kernel W .

When the field values are available only at a set of N points $\{\mathbf{x}_j\}_{j=1}^N$ scattered across the domain Ω , the convolution integral (1) can be approximated using a summation

$$f_h(\mathbf{x}) = \sum_{j \in \mathcal{N}(\mathbf{x})} \frac{m_j}{\rho_j} f(\mathbf{x}_j) W(\mathbf{x} - \mathbf{x}_j, h) \approx \widehat{f}(\mathbf{x}), \quad (2)$$

where m_j and ρ_j represent the mass and density of the j -th particle, respectively, and their ratio is equivalent to the volume associated with the j -th particle, V_j . The volume occupied by each particle can be obtained from the Voronoi tessellation of the particle distribution. One possible simplification involves calculating the volume of a spheroid with a radius equals to the average distance between particles. The notation $\mathcal{N}(\mathbf{x})$ indicates a set of neighbouring particles lying inside the kernel support centred at \mathbf{x} , see the illustration in Figure 1.

Assuming the kernel is suitably smooth, the gradient of the approximation can be obtained by convolving with the kernel gradient, i.e.,

$$\nabla f_h(\mathbf{x}) = \sum_{j \in \mathcal{N}(\mathbf{x})} \frac{m_j}{\rho_j} f(\mathbf{x}_j) \nabla W(\mathbf{x} - \mathbf{x}_j, h). \quad (3)$$

Higher-order derivatives can be obtained similarly using higher-order derivatives of the kernel. Due to the radial definition of the kernel, a chain rule is required to obtain the derivative with respect to the coordinate axes. While it is possible to evaluate the approximant (2) at any point in the domain $\mathbf{x} \in \Omega$, in SPH, the focus is often on evaluating at a point belonging to the particle set $\mathbf{x}_i \in \{\mathbf{x}_j\}$, see Figure 1. In this case, the approximation at \mathbf{x}_i becomes

$$f_h(\mathbf{x}_i) = \sum_{j \in \mathcal{N}(\mathbf{x}_i)} V_j f(\mathbf{x}_j) W_i(\mathbf{x}_j). \quad (4)$$

Here, we introduce a simplified notation $W_i(\mathbf{x}_j)$ for $W(\mathbf{x}_i - \mathbf{x}_j)$. The set of neighbouring points within the support of the kernel centred at \mathbf{x}_i is indicated as $\mathcal{N}(\mathbf{x}_i)$. These compact notations will be used throughout the remainder of the paper.

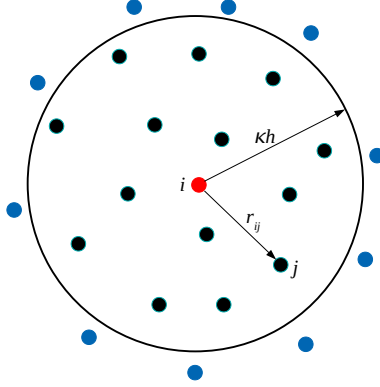


Figure 1: Support of the kernel centred at the i -th particle, which is a circle in \mathbb{R}^2 with radius $R = \kappa h$. The neighbouring particles lying inside the support is coloured black.

2.2. Corrected SPH discretisation

The approximation introduced in (4) does not inherently ensure the reproduction of constant and linear functions across the domain. To achieve such linear polynomial reproducibility, the following criteria must be met

$$\sum_{j \in N(x_i)} V_j W_i(\mathbf{x}_j) = 1 \quad (5a)$$

$$\sum_{j \in N(x_i)} V_j (\mathbf{x}_i - \mathbf{x}_j) W_i(\mathbf{x}_j) = \mathbf{0}. \quad (5b)$$

The first criterion (5a) is the discrete manifestation of the kernel's unit volume, which ensures the reproduction of any constant function. Additionally, satisfying both conditions (5a) and (5b) ensures the reproducibility of any linear function. In SPH, it is common practice to modify the smoothing kernel by introducing correction terms and imposing these linear reproducibility criteria. Following [16, 65], the kernel correction is given by

$$\tilde{W}_i^1(\mathbf{x}_j) = \alpha_i \left(1 + \boldsymbol{\beta}_i \cdot (\mathbf{x}_i - \mathbf{x}_j) \right) W_i(\mathbf{x}_j). \quad (6)$$

Substituting the definition of the corrected kernel (6) into the criterion in (5b) yields the corrective term $\boldsymbol{\beta}_i$, that is,

$$\boldsymbol{\beta}_i = \left(\sum_{j \in N(x_i)} V_j (\mathbf{x}_i - \mathbf{x}_j) \otimes (\mathbf{x}_i - \mathbf{x}_j) W_i(\mathbf{x}_j) \right)^{-1} \sum_{j \in N(x_i)} V_j (\mathbf{x}_j - \mathbf{x}_i) W_i(\mathbf{x}_j). \quad (7)$$

Consecutively, the term α_i is obtained by substituting the computed (7) into the definition (6) and the criterion (5a), resulting in

$$\alpha_i = \frac{1}{\sum_{j \in N(x_i)} V_j W_i(\mathbf{x}_j) \left(1 + \boldsymbol{\beta}_i \cdot (\mathbf{x}_i - \mathbf{x}_j) \right)}. \quad (8)$$

The gradient of the first degree corrected kernel, $\nabla \tilde{W}_i^1(\mathbf{x}_j)$, can be obtained explicitly through multiple application of chain rule [17]. The procedure to obtain $\nabla \tilde{W}_i^1(\mathbf{x}_j)$ is detailed in [Appendix A](#). The gradient $\nabla \tilde{W}_i^1(\mathbf{x}_j)$ satisfies the following criteria [19]

$$\sum_{j \in N(x_i)} V_j \nabla W_i(\mathbf{x}_j) = \mathbf{0} \quad (9a)$$

$$\sum_{j \in N(x_i)} V_j (\mathbf{x}_j - \mathbf{x}_i) \otimes \nabla W_i(\mathbf{x}_j) = \mathbf{I}. \quad (9b)$$

It is important to note that the corrective terms α_i and β_i need to be evaluated at every particle. Moreover, to obtain β_i , an inversion of small matrix is required at every particle.

One possible simplification involves modifying the kernel to only satisfy the zero-th order reproducibility (5a), which is equivalent with setting the term $\beta_i = \mathbf{0}$, and subsequently impose an additional criterion on the gradient. This approach leads to a simpler form of the kernel

$$\tilde{W}_i^0(\mathbf{x}_j) = \frac{W_i(\mathbf{x}_j)}{\sum_{j \in \mathcal{N}(\mathbf{x}_i)} V_j W_i(\mathbf{x}_j)}. \quad (10)$$

The gradient of the zero-th order corrected kernel, $\nabla \tilde{W}_i^0(\mathbf{x}_j)$, does not satisfy the criterion (9b). To address this, a widely adopted approach is to introduce a gradient correction matrix L_i to modify the gradient [19],

$$\tilde{\nabla} \tilde{W}_i^0(\mathbf{x}_j) = L_i \nabla \tilde{W}_i^0(\mathbf{x}_j), \quad (11)$$

such that criterion (9b) is satisfied. The correction matrix L_i can be obtained by substituting the above definition (11) into the criterion (9b), i.e.,

$$L_i = \left(\sum_{j \in \mathcal{N}(\mathbf{x}_i)} V_j (\mathbf{x}_j - \mathbf{x}_i) \otimes \nabla \tilde{W}_i^0(\mathbf{x}_j) \right)^{-1}. \quad (12)$$

The term $\nabla \tilde{W}_i^0(\mathbf{x}_j)$ in (11) and (12) can be obtained by differentiating (10), resulting in

$$\nabla \tilde{W}_i^0(\mathbf{x}_j) = \frac{\nabla W_i(\mathbf{x}_j) - \gamma(\mathbf{x}_j)}{\sum_{j \in \mathcal{N}(\mathbf{x}_i)} V_j W_i(\mathbf{x}_j)}, \quad (13)$$

where

$$\gamma(\mathbf{x}_j) = \frac{\sum_{j \in \mathcal{N}(\mathbf{x}_i)} V_j \nabla W_i(\mathbf{x}_j)}{\sum_{j \in \mathcal{N}(\mathbf{x}_i)} V_j W_i(\mathbf{x}_j)}. \quad (14)$$

It is noteworthy that the resulted gradient (13) satisfies both criteria (9a) and (9b). This approach is often preferred especially when the discretisation of the governing equations only requires the gradient of the kernel, and not the kernel itself.

As an illustrative example, we visualise the kernel and its gradient in a one-dimensional domain $\Omega = (0, 2) \in \mathbb{R}^1$ with a uniformly distributed set of $N = 200$ particles, considering the different types of correction discussed in this section. For the smoothing kernel $W(x)$, we opt for a cubic B-spline with the support size $\kappa h = 1$. In this context, we compare the original (uncorrected) kernel $W_i(\mathbf{x}_j)$, zero-th order corrected kernel $\tilde{W}_i^0(\mathbf{x}_j)$, and first order corrected kernel $\tilde{W}_i^1(\mathbf{x}_j)$, along with their respective first derivatives. Specifically, we investigate the gradient of the original kernel $\nabla W_i(\mathbf{x}_j)$, the corrected gradient of the original kernel $\tilde{\nabla} W_i(\mathbf{x}_j)$, the gradient of the zero-th order corrected kernel $\nabla \tilde{W}_i^0(\mathbf{x}_j)$, the corrected gradient of the zero-th order corrected kernel $\tilde{\nabla} \tilde{W}_i^0(\mathbf{x}_j)$, and finally the gradient of the first order corrected kernel $\nabla \tilde{W}_i^1(\mathbf{x}_j)$.

At $x_i = 1$, Figure 2(a) displays the kernels and their gradients are shown in 2(b). It is observed that in the region far from the boundary, the three kernels overlap, as shown in Figure 2(a). Figure 2(b) shows that all the gradient variants share the same values and exhibit antisymmetry. However, at the boundary, distinct shapes are evident in the kernels as shown in Figure 2(c) for $x_i = 0$. Notably, the first order corrected kernel $\tilde{W}_i^1(\mathbf{x}_j)$ is no longer strictly positive and exhibits a higher peak than the other two variants. Additionally, all three kernels still satisfy the unit volume criterion 5a and display asymmetry when x_i is near the boundary. In 2(d), the gradient $\nabla \tilde{W}_i^1(\mathbf{x}_j)$ exhibits the highest peak at $x_i = 0$ and has two inflection points, while all of the gradient variants are no longer antisymmetric. Finally, it is important to note that higher order consistent kernels (and their respective derivatives) generally entail more involved computations. Therefore, in practice, the choice of the correction technique is often justified based on computational cost and the required accuracy.

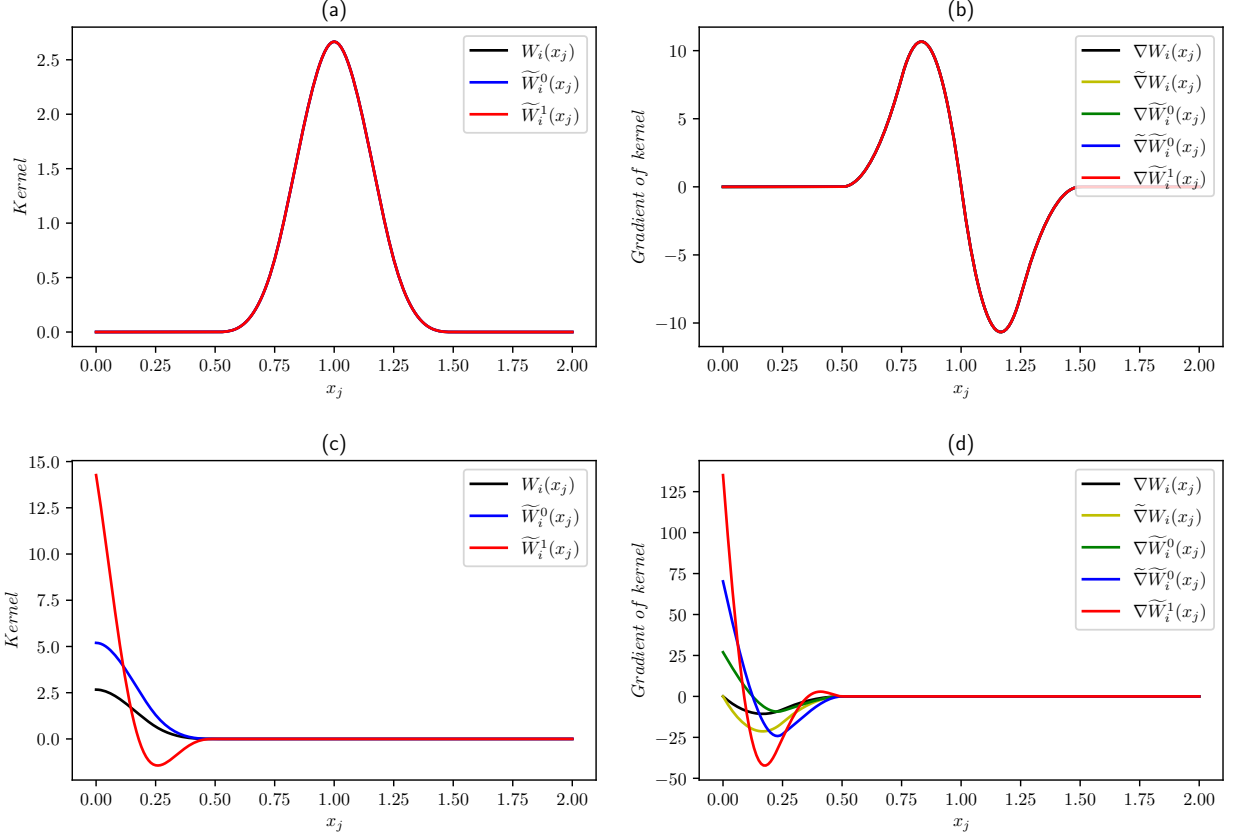


Figure 2: The kernel and kernel gradient of particle i due to interaction with particle j : (a) kernel value, and (b) gradient of kernel at $x_i = 1$. (c) kernel value, and (d) gradient of kernel at $x_i = 0$.

3. Total Lagrangian SPH for solid body

In this section we describe the motion and deformation of an arbitrary solid body and establish the relationship between the current and reference configurations. We then proceed to derive the conservation laws in the reference configuration, closely following the total Lagrangian SPH formulation introduced in [62]. Additionally, we discuss in this section the Jameson-Schmidt-Turkel (JST) technique employed to control dissipation in our dynamic simulations, and describe the explicit three-stage time integrator which relaxes the restriction on the time discretisation.

3.1. Motion and deformation

For clarity in our discussion, in this section we describe the motion and deformation of an arbitrary solid body $\Omega \in \mathbb{R}^3$, as depicted in Figure 3. The current configuration of the body, denoted as Λ , is derived from the displacement and deformation relative to the initial configuration Λ_o . In our notation, we use uppercase \mathbf{X} to represent vector coordinates in the initial configuration and lowercase \mathbf{x} in the current configuration. The mapping between the initial and current configurations is denoted as $\xi(\mathbf{X}, t)$. It is important to note that this mapping encompasses both the displacement and deformation between the two considered configurations. Furthermore, we specifically consider an infinitesimally small region $P \in \Omega$ within the domain with an initial position \mathbf{X} that occupies a new position \mathbf{x} in the current configuration. The relationship between the initial position \mathbf{X} and the current position \mathbf{x} is expressed as

$$\mathbf{x} = \mathbf{X} + \mathbf{u}, \quad (15)$$

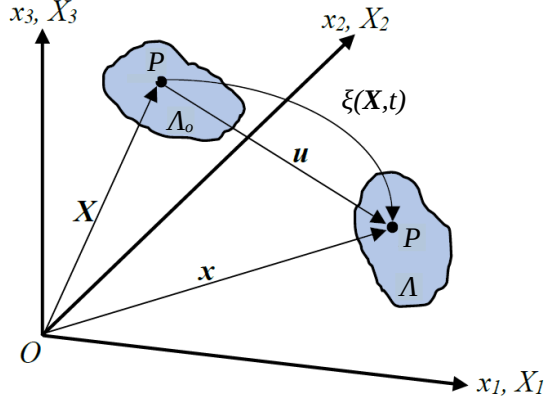


Figure 3: Description of the motion with respect to the initial and current configuration

where the vector \mathbf{u} denotes the displacement of P . Utilising this relationship, we obtain the deformation gradient tensor \mathbf{F} as

$$\mathbf{F} = \frac{d\mathbf{x}}{d\mathbf{X}} = \mathbf{I} + \frac{d\mathbf{u}}{d\mathbf{X}}. \quad (16)$$

Based on the deformation gradient mentioned above, the stress tensor is calculated using a specific constitutive relation, which is dependent on the material type. In our examples, we consider a nearly incompressible hyperelastic Neo-Hookean constitutive model for rubber-like materials. As documented in [66], the first Piola-Kirchhoff stress is decomposed into the summation of the volumetric and deviatoric components

$$\mathbf{P} = \mathbf{P}_{vol} + \mathbf{P}_{dev}. \quad (17)$$

Here, the volumetric and deviatoric stresses are calculated as follows

$$\mathbf{P}_{vol} = pJ\mathbf{F}^{-\top} \quad (18a)$$

$$\mathbf{P}_{dev} = \mu J^{-2/3} \left(\mathbf{F} - \frac{1}{3}(\mathbf{F} : \mathbf{F})\mathbf{F}^{-\top} \right). \quad (18b)$$

In these expressions, $p = \kappa(J - 1)$ represents the hydrostatic pressure, μ is the shear modulus, κ is the bulk modulus, and the Jacobian J is the determinant of the deformation gradient tensor, i.e., $J = \det(\mathbf{F})$. The relation between the first Piola-Kirchhoff stress \mathbf{P} and the Cauchy stress $\boldsymbol{\sigma}$ is established by

$$\boldsymbol{\sigma} = \frac{1}{J}\mathbf{P} \cdot \mathbf{F}^{\top}. \quad (19)$$

Note that the continuum assumption is employed throughout the derivation in this section. The discretisation of the continuous fields using particles, as described in Section 2, will be discussed in the upcoming sections.

3.2. Total Lagrangian formulation of conservation laws

In the total Lagrangian formulation, the initial configuration is used to describe the motion and deformation of the solid body. The conservation of linear momentum relative to the initial configuration is described as

$$\frac{d\mathbf{p}}{dt} - \text{div}(\mathbf{P}) = \mathbf{s}_o. \quad (20)$$

Here \mathbf{p} denotes the momentum per unit of undeformed volume, s_o represents the source of force per unit of undeformed volume, and \mathbf{P} is the first Piola-Kirchhoff stress. The subscript o is used to indicate that the fields and their derivatives are associated with the reference, or undeformed, configuration Λ_o . We discretise the stress field according to the SPH discretisation introduced in Section 2, resulting in

$$\frac{d\mathbf{p}_i}{dt} = s_{o,i} + \sum_{j \in \mathcal{N}(X_i)} V_{o,j} \mathbf{P}_j \nabla_o \tilde{W}_i^1(X_j). \quad (21)$$

Here X_j indicates the position of the j -th particle in the initial configuration, and $V_{o,j}$ denotes the undeformed volume of the j -th particle. In (21), we adopt a common approximation of derivative in SPH and the gradient of the first-degree corrected kernel $\nabla_o \tilde{W}_i^1(X_j)$ is applied to ensure the zero-th and first order completeness.

It is important to note at this stage that, following the correction, the value of the kernel gradient is no longer anti-symmetric, i.e., $\nabla_o \tilde{W}_i^1(X_j) \neq -\nabla_o \tilde{W}_j^1(X_i)$. The direct implication of this property is that the interaction forces between two particles are not the same in the pairwise direction and, therefore, do not, in general, satisfy the conservation of linear momentum [17]. In this work, we introduce \mathbf{P}_i and modify the corrected kernel gradient to conserve the total linear momentum of the system, as also proposed in [17, 21]. The conservation of momentum can be written using the modified gradient

$$\frac{d\mathbf{p}_i}{dt} = s_{o,i} + \frac{1}{2} \sum_{j \in \mathcal{N}(X_i)} V_{o,j} (\mathbf{P}_i + \mathbf{P}_j) (\nabla_o \tilde{W}_i^1(X_j) - \nabla_o \tilde{W}_j^1(X_i)). \quad (22)$$

The formulations in (22) ensure pairwise antisymmetric interaction forces, yielding linear momentum preservation. Following [60], the additional relation used here is the conservation of the deformation gradient \mathbf{F} , governed by

$$\frac{d\mathbf{F}}{dt} - \nabla_o \left(\frac{1}{\rho_o} \mathbf{p} \otimes \mathbf{I} \right) = \mathbf{0}. \quad (23)$$

Note that (23) can be interpreted as an alternative manifestation of mass conservation. The discrete form of (23) is again obtained using the SPH discretisation,

$$\frac{d\mathbf{F}_i}{dt} = \sum_{j \in \mathcal{N}(X_i)} \frac{V_{o,j}}{\rho_{o,j}} \mathbf{p}_j \otimes \nabla_o \tilde{W}_i^1(X_j). \quad (24)$$

We reiterate here that the use of the gradient of the first order corrected kernel $\nabla_o \tilde{W}_i^1(X_j)$ ensures that linear field can be reproduced and its respective gradient can be exactly computed up to machine precision [17].

In our solid dynamics simulations, we use the Jameson-Schmidt-Turkel (JST) method [61, 62] to suppress the presence of excessive dissipation commonly observed in cases involving large strain. The JST method introduces an additional term $\mathbf{D}(\mathbf{p})$ in terms of the momentum field \mathbf{p} into (22), resulting in,

$$\frac{d\mathbf{p}_i}{dt} = s_{o,i} + \frac{1}{2} \sum_{j \in \mathcal{N}(X_i)} V_{o,j} (\mathbf{P}_i + \mathbf{P}_j) (\nabla_o \tilde{W}_i^1(X_j) - \nabla_o \tilde{W}_j^1(X_i)) + \mathbf{D}(\mathbf{p}), \quad (25)$$

where $\mathbf{D}(\mathbf{p})$ consists of two terms involving harmonic and biharmonic operators

$$\mathbf{D}(\mathbf{p}) = \eta^{(2)} C_p h \sum_{j \in \mathcal{N}(X_i)} V_{o,j} (\mathbf{p}_j - \mathbf{p}_i) \tilde{\nabla}_o^2 W_i(X_j) - \eta^{(4)} C_p h^3 \sum_{j=1}^{N_i} V_{o,j} (\nabla_o^2 \mathbf{p}_j - \nabla_o^2 \mathbf{p}_i) \tilde{\nabla}_o^2 W_i(X_j). \quad (26)$$

The constant C_p denotes the speed of p -wave travelling through the material [63] and the parameter h denotes the minimum smoothing length within the entire domain. In most of our dynamic simulations, we use the constants $\eta^{(2)} = 0$ and $\eta^{(4)} = 0.125$ according to [62].

Further inspection of the equation (26) indicates that the Laplacian term must satisfy completeness. For the second derivative of the kernel to reproduce a constant function, the kernel must satisfy second-order completeness, which is often deemed computationally prohibitive. In this work, we adopt the correction for the Laplacian term following the

approach in [16], resulting in the term $\tilde{\nabla}_o^2 W_i(\mathbf{X}_j)$. The resulting corrected Laplacian of the kernel sufficiently ensures that the second derivative is zero for linear and constant fields, and constant for a quadratic field. To evaluate the term $\nabla_o^2 \mathbf{p}_i$ in (26), we expand with SPH discretisation involving the corrected Laplacian $\tilde{\nabla}_o^2 W_i(\mathbf{X}_j)$, i.e.,

$$\nabla_o^2 \mathbf{p}_i = \sum_{j \in N(\mathbf{X}_i)} V_{o,j}(\mathbf{p}_j - \mathbf{p}_i) \tilde{\nabla}_o^2 W_i(\mathbf{X}_j). \quad (27)$$

Furthermore, we note that the corrected Laplacian of the kernel is not symmetric, i.e., $\tilde{\nabla}_o^2 W_i(\mathbf{X}_j) \neq \tilde{\nabla}_o^2 W_j(\mathbf{X}_i)$, which can affect the preservation of linear momentum. To address this concern, we use the average Laplacian for each particle pair, leading to the final expression of $\mathbf{D}(\mathbf{p})$

$$\begin{aligned} \mathbf{D}(\mathbf{p}) = & \frac{1}{2} \eta^{(2)} C_p h \sum_{j \in N(\mathbf{X}_i)} V_{o,j}(\mathbf{p}_j - \mathbf{p}_i) (\tilde{\nabla}_o^2 W_i(\mathbf{X}_j) + \tilde{\nabla}_o^2 W_j(\mathbf{X}_i)) - \\ & \frac{1}{2} \eta^{(4)} C_p h^3 \sum_{j \in N(\mathbf{X}_i)} V_{o,j}(\nabla_o^2 \mathbf{p}_j - \nabla_o^2 \mathbf{p}_i) (\tilde{\nabla}_o^2 W_i(\mathbf{X}_j) + \tilde{\nabla}_o^2 W_j(\mathbf{X}_i)). \end{aligned} \quad (28)$$

Our final component in formulating the total Lagrangian SPH involves time integration. To illustrate our strategy, we define the rate of change of a generic particle property \mathbf{U} as

$$\frac{d\mathbf{U}}{dt} = R(\mathbf{U}, t). \quad (29)$$

An example of the particle property \mathbf{U} is the linear momentum \mathbf{p} . In this case, the above expression resembles equation (25), where here R indicates the right hand side operator. In this work, we employ the explicit three-stage time integrator to update the particle property \mathbf{U} at every time step [63],

$$\mathbf{U}^* = \mathbf{U}^n + R(\mathbf{U}^n, t^n) \Delta t \quad (30a)$$

$$\mathbf{U}^{**} = \frac{3}{4} \mathbf{U}^n + \frac{1}{4} (\mathbf{U}^* + R(\mathbf{U}^*, t^n) \Delta t) \quad (30b)$$

$$\mathbf{U}^{n+1} = \frac{1}{3} \mathbf{U}^n + \frac{2}{3} (\mathbf{U}^{**} + R(\mathbf{U}^{**}, t^n) \Delta t). \quad (30c)$$

The time increment $\Delta t = t^{n+1} - t^n$ is calculated based on the Courant-Friedrichs-Lewy (CFL) condition

$$\Delta t = \alpha_{CFL} \cdot \min \left(\frac{r_{ij}}{C_{p,max}} \right), \quad (31)$$

where $r_{ij} = \|\mathbf{x}_i - \mathbf{x}_j\|$ is the distance between particle i and j with respect to the current configuration, and $C_{p,max}$ is the maximum p -wave speed. The constant α_{CFL} is commonly case dependent, but our default setting is as high as $\alpha_{CFL} = 0.9$.

4. Alternative formulation for computing deformation gradient

Spurious non-physical oscillations, namely the zero-energy mode or hourglass mode, have been observed in various computational methods including finite difference, finite elements, and particle method like SPH. These oscillations can be understood as the manifestation of displacement without any corresponding strain. In the context of SPH, this phenomenon arises due to the inaccurate computation of gradients of the field, allowing for zero gradients not strictly associated with constant fields. Motivated by this insight, we elaborate on our proposed alternative for computing the deformation gradient with improved accuracy to suppress the presence of the zero-energy mode. In this section, we begin by outlining our approach in a one-dimensional setting and subsequently integrate this idea into the total Lagrangian SPH framework in higher dimensions.

4.1. One-dimensional illustration

For clarity and simplicity of the discussion, we illustrate our approach in a one-dimensional setting. Consider the domain $\Omega \in \mathbb{R}^1$ in the reference configuration, where we assume that the deformation field can be obtained at a finite set of particles with coordinates $X_j \in \Omega$. The deformation gradient at a specific particle X_i can be obtained using the SPH discretisation scheme as discussed in Section 2,

$$\frac{dx}{dX}(X_i) \approx \sum_{j \in \mathcal{N}(X_i)} \frac{dW(X_i - X_j, h)}{dX} V_j x_j. \quad (32)$$

The notation $\mathcal{N}(X_i)$ denotes the list of particle indices belonging to the neighbourhood of X_i . The observation of zero-energy, or hourglass, mode in SPH is attributed to the discrete approximation of the deformation gradient, which permits it to be zero not strictly for a constant deformation field. This observation motivates the development of methods that redefine the gradient computation in SPH using an additional set of particles, known as stress points [32, 51, 52].

Another possible formulation of the field derivative can be defined using the gradient of deformation obtained at the particles and the kernel W , in contrast to the standard SPH formulation in (32), i.e.,

$$\frac{dx}{dX}(X_i) \approx \sum_{j \in \mathcal{N}(X_i)} V_j W(X_i - X_j, h) \left(\frac{dx}{dX} \right)_{ij}. \quad (33)$$

This alternative formulation can be traced back to the application of a differential operator D to the convolution between two continuous functions W and x , which leads to $D(W * x) = D W * x = W * D x$. Note that in our one dimensional illustration, the operator D is d/dX . A geometric interpretation of (33) is that the deformation gradient at particle X_i is approximated by a weighted average of the gradient measured between X_i and its neighbour X_j . This pairwise gradient can be simply defined as

$$\left(\frac{dx}{dX} \right)_{ij} = \frac{x_j - x_i}{X_j - X_i}. \quad (34)$$

The above equation provides an estimate for the derivative between X_i and the neighbouring particles at X_j , implicitly requiring the index $j \neq i$ to avoid a zero denominator. This approach can also be viewed as a *bond-based* gradient estimation, as proposed in peridynamics [58, 59, 67]. While the presented formulation in (34) is straightforward, it lacks precision when approximating the gradient, even for a linear field $x = X + 1$, as illustrated in Figure 4. Notably, even in regions distant from the boundary, the estimated gradient does not equate to 1, stemming from the omission of the gradient estimate at X_i .

Building on the aforementioned observation, we introduce an improved formulation of the bond-based gradient $\left(\frac{dx}{dX} \right)_{ij}$ by considering the gradient estimate at particle X_i ,

$$\left(\frac{dx}{dX} \right)_{ij} = \begin{cases} \frac{x_j - x_i}{X_j - X_i} & \text{if } j \neq i \\ \sum_{j \in \mathcal{N}(X_i)} \frac{dW(X_i - X_j, h)}{dX} V_j x_j & \text{if } j = i. \end{cases} \quad (35)$$

Note that for $i = j$, we adopt the standard gradient estimate in SPH (32). This formulation can also be viewed as a correction of (32) evaluated at X_i by considering the pairwise deformation gradient with its neighbours. As a preliminary assessment, we consider a uniform particle distribution in one-dimensional domain $\Omega = (0, 5)$ with spacing $\Delta x = 1/8$. Our objective is to approximate the gradient of the deformation field $x = X + 1$ using the standard formula (32), the bond-based estimate (34), and the improved formulation (35). Here we consider a cubic b-spline kernel with first order correction with half-width $R = 4 \Delta x$. As depicted in Figure 4(b), the bond-based estimate (34) exhibits discrepancy with the expected value. However, the proposed improvement to the bond-based formulation, as described in (35), yields a correct deformation gradient of 1 as also achieved by the standard SPH described in (32).

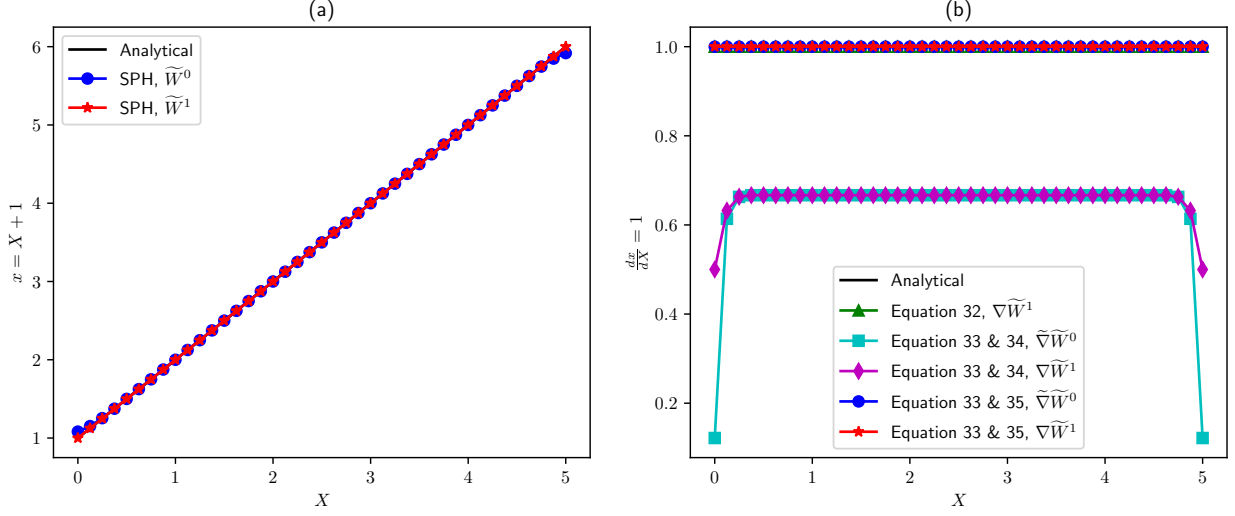


Figure 4: Field reconstruction from point values: (a) deformation , (b) deformation gradient.

A more detailed analysis is conducted by calculating the deformation gradient of higher-order deformation fields. Specifically, our focus lies on comparing the standard SPH formula (32) using the gradient of first-order corrected kernel $\nabla \tilde{W}^1$, and our proposed formula (35) with two variants of kernel gradients $\nabla \tilde{W}^1$ and $\tilde{\nabla} \tilde{W}^0$. Here we use the notation ∇ for a comparable referencing with Section 2.2. The deformation gradients of quadratic and cubic polynomial deformation fields are presented in Figure 5. The results indicate that for higher polynomial orders, the standard SPH (32) exhibits errors due to the maximum polynomial reproducibility being only up to linear. The elimination of this error requires satisfying higher-order conditions, demanding more intensive computational efforts. It is also evident from (35) that the proposed formulation significantly improves accuracy, especially in proximity to the boundary.

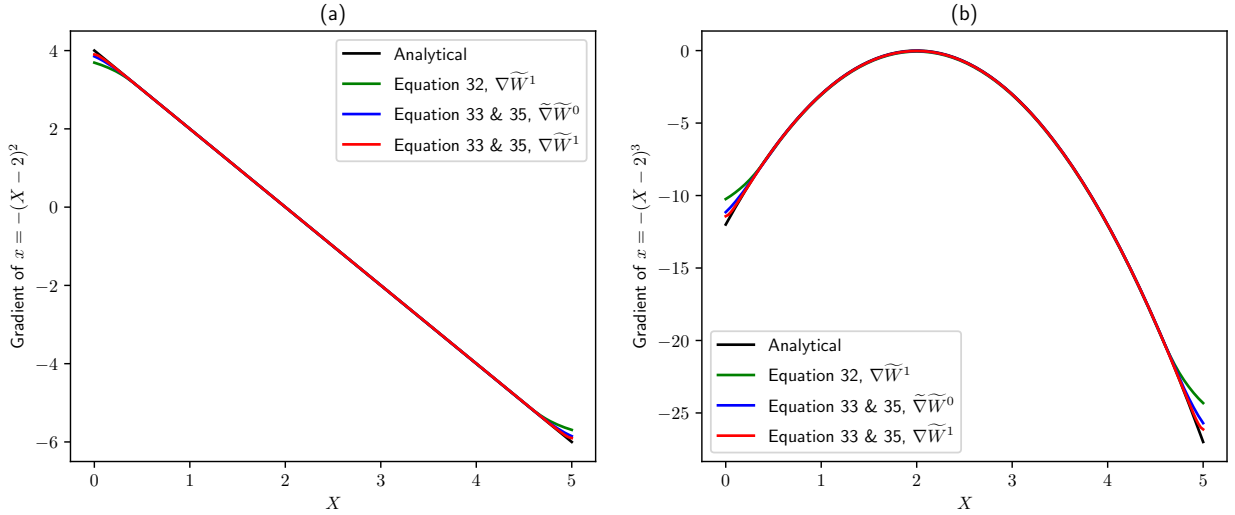


Figure 5: Gradient approximation of a deformation field from point values: (a) quadratic function, (b) cubic function

Next, we assess the convergence of error in estimating the deformation gradient with respect to spatial refinement. As the deformation field, we employ cubic $x = X^3 + 1$ and periodic $x = \sin(5X)$ functions. Figure 6 shows the root

mean square error (RMSE) of the deformation gradient with respect to the analytical solutions. It is evident that the RMSE of classical SPH 32 does not decrease as h is refined and more particles are involved. In contrast, reduction of error is observed for the proposed formulation 35, with the one using $\nabla \tilde{W}^1$ exhibiting lower error than the one using $\nabla \tilde{W}^0$. This discrepancy is less emphasised when dealing with oscillatory functions. This justifies that the proposed improved bond-based formulation significantly improves the estimation of the deformation gradient from the field values obtained at the particles.

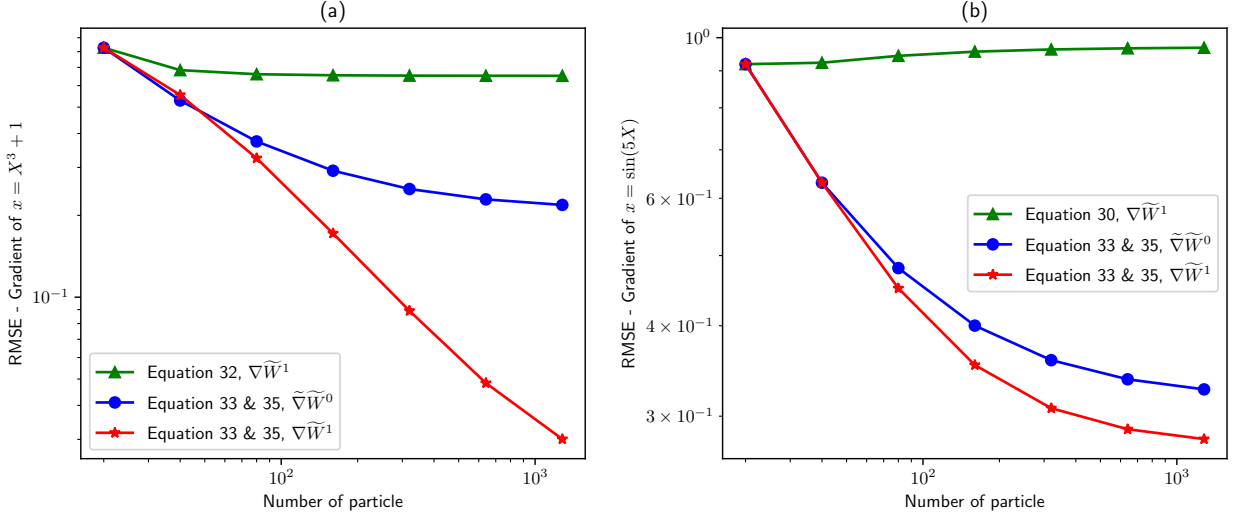


Figure 6: RMSE analysis of the SPH approximation: (a) gradient of cubic function, (b) gradient of sinusoidal function

4.2. SPH implementation of the proposed deformation gradient

In this section we extend the one-dimensional formulation of the improved bond-based deformation gradient (35) to higher dimensions and describe its implementation in our TLSPH framework, as described in Section 3. As a preliminary reminder, in our TLSPH, the deformation gradient at each particle \mathbf{F}_i is computed at every time step by first evaluating the conservation of the deformation gradient (24), and subsequently integrating over a time step Δt . Following the evaluation of \mathbf{F}_i , the modified deformation gradient \mathbf{F}_i^c is then obtained analogous to the one-dimensional expression (33),

$$\mathbf{F}_i^c = \sum_{j \in \mathcal{N}(\mathbf{X}_i)} V_j W(\mathbf{X}_j - \mathbf{X}_i, h) \mathbf{F}_{ij}. \quad (36)$$

One possible expression for the bond-based deformation gradient \mathbf{F}_{ij} can be obtained purely from kinematics information, serving as a direct extension from our one-dimensional illustration,

$$\mathbf{F}_{ij} = \begin{cases} \frac{\mathbf{x}_j - \mathbf{x}_i}{r_{o,ij}} \otimes \frac{\mathbf{X}_j - \mathbf{X}_i}{r_{o,ij}} & \text{if } j \neq i \\ \mathbf{F}_i & \text{if } j = i \end{cases}. \quad (37)$$

The term $r_{o,ij}$ indicates the Euclidian distance between particle i and j in the initial configuration, i.e., $\|\mathbf{X}_j - \mathbf{X}_i\|$. The interparticle component $\frac{\mathbf{x}_j - \mathbf{x}_i}{r_{o,ij}} \otimes \frac{\mathbf{X}_j - \mathbf{X}_i}{r_{o,ij}}$ is rank deficient. An alternative expression for the interparticle deformation gradient (i.e., when $j \neq i$) is proposed in [59] by correcting the *averaged* deformation gradient \mathbf{F}_i projected to each bond with the actual deformation (37), which reads

$$\mathbf{F}_{ij} = \begin{cases} \mathbf{F}_i - \left(\left(\mathbf{F}_i \cdot \frac{\mathbf{X}_j - \mathbf{X}_i}{r_{o,ij}} \right) \otimes \frac{\mathbf{X}_j - \mathbf{X}_i}{r_{o,ij}} \right) + \left(\frac{\mathbf{x}_j - \mathbf{x}_i}{r_{o,ij}} \otimes \frac{\mathbf{X}_j - \mathbf{X}_i}{r_{o,ij}} \right) & \text{if } j \neq i \\ \mathbf{F}_i & \text{if } j = i \end{cases}. \quad (38)$$

The bond-based deformation gradient (when $i \neq j$) is full-rank and computationally efficient [59]. In (38), the component along the bond direction of the *averaged* deformation gradient \mathbf{F}_i is first removed and then corrected with the actual deformation gradient between the two particles, which is $\frac{\mathbf{x}_j - \mathbf{x}_i}{r_{o,ij}} \otimes \frac{\mathbf{x}_j - \mathbf{x}_i}{r_{o,ij}}$. Note that this expression is still consistent with (35) since $\frac{X_j - X_i}{r_{o,ij}} = 1$ in one-dimension. Our final note concerns the computation of the particle deformation \mathbf{x}_i . In this work we obtain \mathbf{x}_i from the momentum update (25) per unit mass, and subsequently performing time integrations. Note that obtaining \mathbf{x}_i by integrating \mathbf{F}_i will not capture the real deformation due to the weighted averaging applied in (24).

5. Numerical examples

We present in this section several numerical experiments with increasing complexity to investigate the convergence property and the performance of the improved bond-based deformation gradient formulation proposed in this work. Our first analysis focuses on the convergence of L_2 -norm and H_1 -seminorm errors in the displacement field using a two-dimensional swinging plate example. Within this study, we also investigate the effect of the kernel width as well as the correction type on the convergence. Additionally, we study the preservation of energy, linear momentum, and angular momentum through various two- and three-dimensional problems. These examples demonstrate that the proposed method improves numerical stability, enabling computations involving larger strains.

5.1. Convergence analysis using swinging plate problem

First, we investigate the convergence of the solution to the swinging plate problem [40, 41, 62, 68] in L_2 -norm and H_1 -seminorm errors of the displacement field. The domain is a square plate $\Omega \in \mathbb{R}^2$ with a width of 2 m. We consider a rubber-like material characterised by a nearly-incompressible Neo-Hookean constitutive model with a uniform Young's modulus $E = 17$ MPa, Poisson's ratio $\nu = 0.495$, and density $\rho_o = 1100$ kg/m³. The displacement normal to the boundaries is constrained, as illustrated in Figure 7. An initial velocity is applied to the system at time $t = 0$, which is derived from a prescribed solution

$$\mathbf{u}(\mathbf{x}, t) = U \sin(\omega t) \begin{Bmatrix} -\sin(\frac{\pi}{2} X_1) \cos(\frac{\pi}{2} X_2) \\ \cos(\frac{\pi}{2} X_1) \sin(\frac{\pi}{2} X_2) \end{Bmatrix}, \quad (39)$$

where ω represents the angular frequency given by

$$\omega = \frac{\pi}{2} \sqrt{2\mu/\rho_o}. \quad (40)$$

The variable $\mu = \frac{E}{2(1+\nu)}$ is the shear modulus, and the amplitude is chosen as $U = 0.01$ m/s. Analytical solutions for the velocity and displacement gradient can be obtained through differentiation with respect to both time and space.

The L_2 -norm error of the displacement is defined as follows,

$$\|\mathbf{u} - \mathbf{u}_h\| = \left(\int (\mathbf{u} - \mathbf{u}_h) \cdot (\mathbf{u} - \mathbf{u}_h) \, d\Omega \right)^{\frac{1}{2}}, \quad (41)$$

and the H_1 -seminorm error is defined as

$$|\mathbf{u} - \mathbf{u}_h| = \left(\int \left(\frac{\partial \mathbf{u}}{\partial \mathbf{X}} - \frac{\partial \mathbf{u}_h}{\partial \mathbf{X}} \right) : \left(\frac{\partial \mathbf{u}}{\partial \mathbf{X}} - \frac{\partial \mathbf{u}_h}{\partial \mathbf{X}} \right) \, d\Omega \right)^{\frac{1}{2}}, \quad (42)$$

where \mathbf{u}_h represents the numerical displacements. The integrations in 41 and 42 are evaluated numerically using Gauss quadratures. Specifically, the plate is first subdivided into 10×10 tiles, and then 5×5 Gauss points are distributed within each tile.

In this example, we also study the effect of kernel correction on the obtained numerical solutions. Specifically, we consider the zero-th order corrected kernel $\tilde{W}_i^0(\mathbf{X}_j)$ and its corrected gradient $\tilde{\nabla}_0 \tilde{W}_i^0(\mathbf{X}_j)$, as well as the first order corrected kernel $\tilde{W}_i^1(\mathbf{X}_j)$ and its gradient $\tilde{\nabla}_0 \tilde{W}_i^1(\mathbf{X}_j)$, as discussed in Section 2.2. We use a cubic spline kernel with

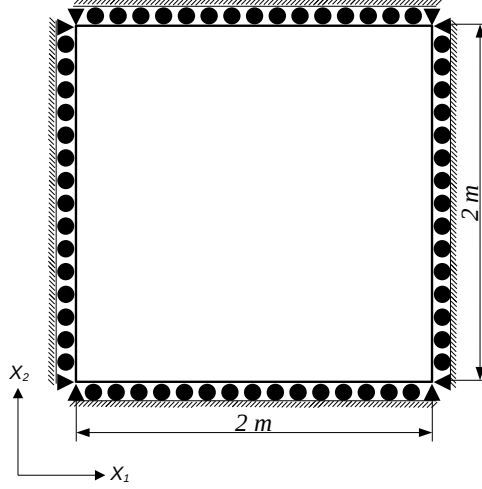


Figure 7: Configuration and dimension of the swinging plate for the convergence test

size defined by a parameter $\beta = h/d$, representing the ratio between the smoothing length h and the particle spacing d . In our simulations, we vary β within the set $\{0.6, 0.9, 1.2, 1.5\}$. The displacement and stress contours are shown in Figure 8. Qualitatively, it is evident that the contours are smooth without non-physical oscillations. Furthermore, the numerical results agrees well with the analytical solutions presented in tiles (a) and (d). The L_2 -norm and H_1 -seminorm errors are shown in Figure 9. Here we consider an initial particle configuration with uniform spacing $d = 0.2$ and successively refine the spacing by a factor of 0.5. The two JST parameters in this example are $\eta^{(2)} = 0$ and $\eta^{(4)} = 0.125$. It is evident that the proposed method yields the optimal convergence rate of 2 in L_2 -norm and 1 in H_1 -seminorm. In the L_2 -norm, the two kernel-gradient pairs lead to the optimal convergence rate of 2, with minimal variations with respect to the parameter β . In the H_1 -seminorm these variations are more emphasised but still roughly yield to convergence rates between 0.9 to 1.2.

5.2. Momentum preservation analysis using spinning plate and cube problems

Next we investigate the preservation of linear and angular momentum using a spinning plate problem, following the example demonstrated in [69], and aim to identify any spurious instability modes in the long-term response. We consider a square plate with width 1 m embedded in \mathbb{R}^3 with initial angular velocity vector $\omega_o = (0, 0, \omega_3)^T$ as depicted in Figure 10. The axis of rotation is placed at the centre of the plate, with $\omega_3 = 105$ rad/s. The initial velocity can be computed as

$$\mathbf{v}_o(\mathbf{X}) = \boldsymbol{\omega}_o \times \mathbf{X}, \quad (43)$$

where $\mathbf{X} = (X_1, X_2, 0)^T$ represents the position in the reference configuration measured from the centre of rotation. We consider a rubber material characterised by a modulus of elasticity $E = 17$ MPa, Poisson's ratio $\nu = 0.45$, and density $\rho_o = 1100$ kg/m³. In this example, we discretise the plate using 200×200 uniformly distributed particles. We choose a cubic b-spline kernel with a smoothing length-to-particle spacing ratio $\beta = 0.9$. Furthermore, in this example we employ the first order kernel correction and its gradient to ensure linear reproducibility.

We qualitatively examine the presence of the spurious oscillations by inspecting the von Mises stress distribution, as presented in Figure 11. In the short term response, up to $t = 0.2$ s, depicted in the first row of Figure 11, the deformation shape obtained through the proposed method aligns with the results documented in [69]. To further assess the performance of our proposed method, we extend the simulation to examine its long term response, reaching up to $t = 2$ s. As evident from the second row of Figure 11, our proposed method endures the extended simulation duration, remaining free from spurious artifacts. This demonstrates stability and robustness over an extended period, reinforcing the efficacy of the proposed approach.

Next we examine the total linear and angular momentum in the system. Given the pure rotational movement of the plate, the total linear momentum should be zero, and the total angular momentum should be determined by the

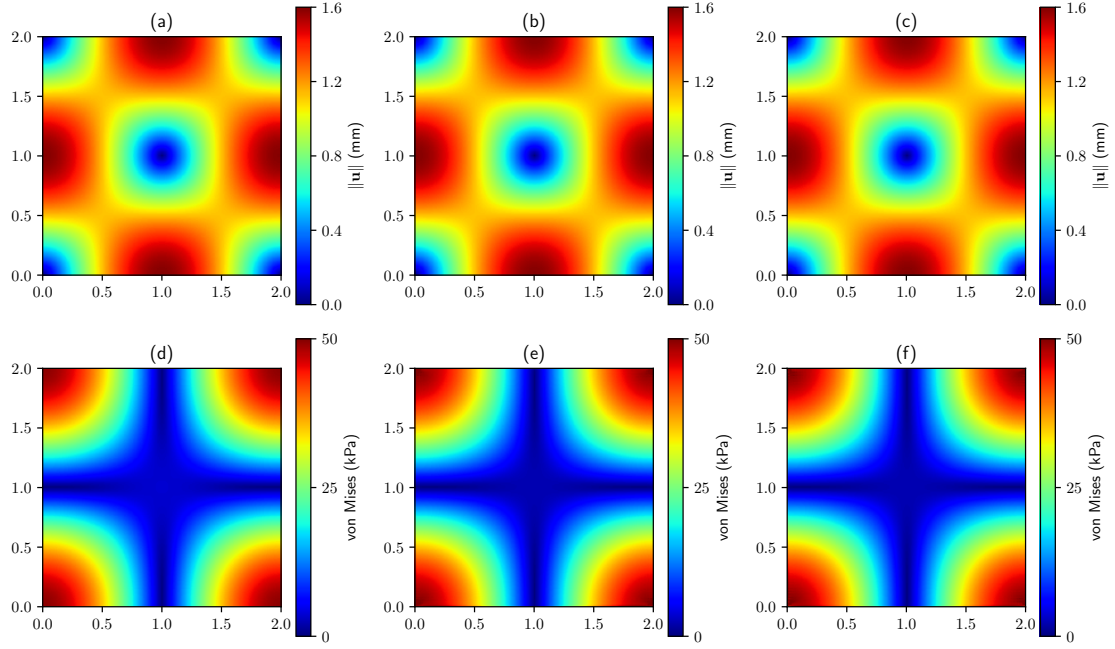


Figure 8: The displacement (m) and von Mises stress (Pa) of the swinging plate: (a) analytical displacement, (b) displacement using $\tilde{W}_i^0(X_j)$ & $\tilde{\nabla}_0 \tilde{W}_i^0(X_j)$, (c) displacement using $\tilde{W}_i^1(X_j)$ & $\tilde{\nabla}_0 \tilde{W}_i^1(X_j)$, (d) analytical von Mises stress, (e) von Mises stress using $\tilde{W}_i^0(X_j)$ & $\tilde{\nabla}_0 \tilde{W}_i^0(X_j)$, (f) von Mises stress using $\tilde{W}_i^1(X_j)$ & $\tilde{\nabla}_0 \tilde{W}_i^1(X_j)$

total of moment of inertia of each particle in the plate multiplied by its angular velocity. These values should remain constant throughout the simulation. As discussed in [19], the preservation of linear momentum is inherent to the kernel correction and its gradient being used. However, preserving angular momentum remains a challenge due to the corrected kernel being asymmetric, which introduces additional moments. To address this issue, we use a denser particle configurations of 200×200 thereby decreasing the moment arm between particle interactions. The total linear and angular momentum for the spinning plate problem is presented in Figure 12. It is evident that our method ensures the preservation of both linear and angular momentum throughout the simulation time.

We extend the example to a three-dimensional rotating cube analogous to the previously discussed spinning plate. The cube has a width of 1 m and the material properties include a modulus of elasticity $E = 17$ MPa, Poisson's ratio $\nu = 0.3$, and density $\rho_o = 1100$ kg/m³, following the example shown in [62]. The cube is discretised using $50 \times 50 \times 50$ particles. We consider the same initial angular velocity as employed in the 2D spinning plate problem. The von Mises stress distribution is presented in Figure 13 from $t = 0$ s to $t = 2$ s. It is evident that the proposed method leads to the stress contour without spurious non-physical oscillation. The total linear and angular momentum of the system are shown in Figure 14. It is observed that the proposed method yields the correct total linear and angular momentum throughout the duration of simulation.

5.3. Energy preservation analysis using finite deformation of a column

In this example we assess the preservation of energy using a square column subjected to an initial velocity, as previously demonstrated in [62]. The dimensions of the column are $1 \times 1 \times 6$ m and it is fixed at the bottom end, as depicted in Figure 15. The physical fields are discretised using $11 \times 11 \times 66$ particles. The smoothing kernel used in this example is a cubic b-spline with smoothing length to particle spacing ratio $\beta = 0.9$. The column is made from a rubber material with modulus of elasticity $E = 17$ MPa, Poisson's ratio $\nu = 0.45$, and density $\rho_o = 1100$ kg/m³. An initial velocity $\mathbf{v}_o = (0, 5X_3/3, 0)^T$ m/s is applied to the beam at time $t = 0$ s.

The deformed shape and the von Mises stress distribution of the column are displayed in Figure 16. It is evident that the stress contours are free from spurious oscillations and qualitatively show agreement with the reference [62].

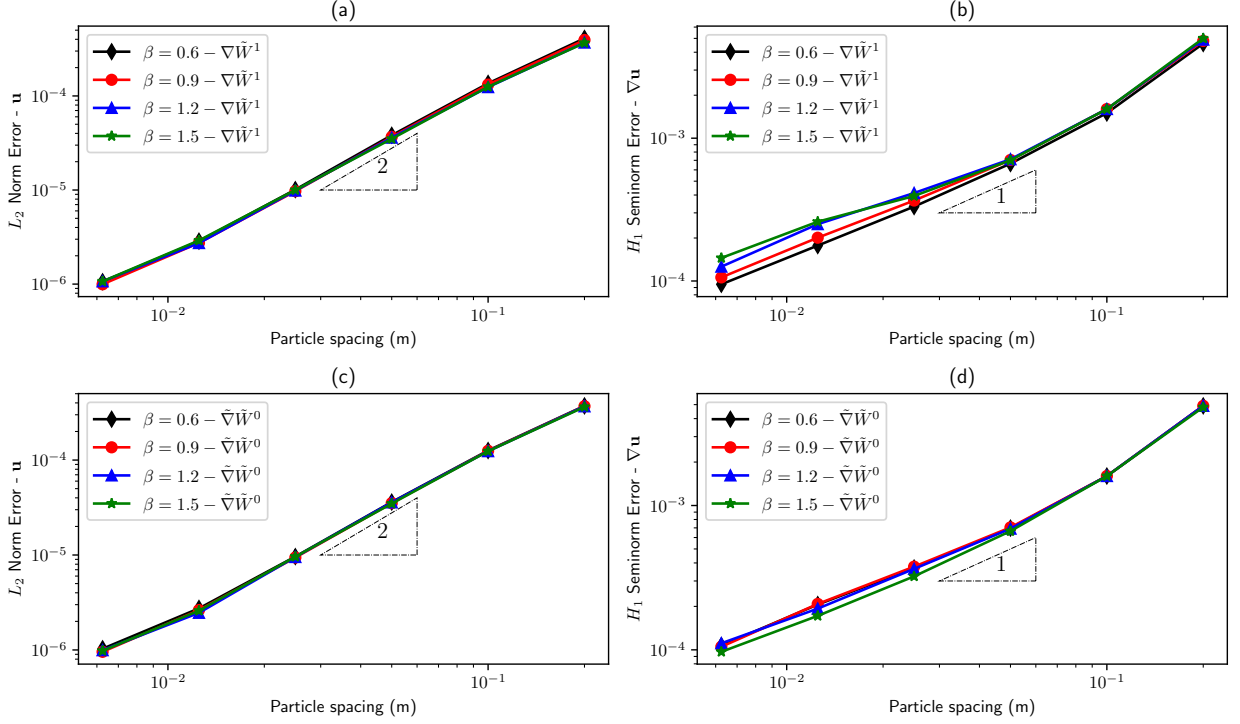


Figure 9: Convergence rate of the proposed SPH: (a) displacement L_2 norm error using $\tilde{W}_i^1(X_j)$ & $\nabla_0 \tilde{W}_i^1(X_j)$, (b) displacement gradient H_1 seminorm error using $\tilde{W}_i^1(X_j)$ & $\nabla_0 \tilde{W}_i^1(X_j)$, (c) displacement L_2 norm error using $\tilde{W}_i^0(X_j)$ & $\nabla_0 \tilde{W}_i^0(X_j)$, (d) displacement gradient H_1 seminorm error using $\tilde{W}_i^0(X_j)$ & $\nabla_0 \tilde{W}_i^0(X_j)$

The total energy of the system can be decomposed into kinetic energy E_k and strain energy W_s where each can be obtained by summing up the individual particle contributions. The particle's kinetic energy is obtained by considering its mass and velocity. The particle's strain energy is determined based on the hyperelastic Neo-Hookean model, i.e.,

$$E_k = \frac{1}{2} \sum_{i=1}^N m_i (\mathbf{v}_i \cdot \mathbf{v}_i) \quad (44a)$$

$$W_s = \sum_{i=1}^N \left(\frac{\mu}{2} (I_{1i} - 3 - 2 \ln J_i) + \frac{\lambda_L}{2} (J_i - 1)^2 \right) \quad (44b)$$

$$E_t = E_k + W \quad (44c)$$

In (44), λ_L represents the first Lamé parameter, μ stands for the shear modulus or the second Lamé parameter. The notation I_1 indicates the first invariant of the right Cauchy-Green deformation tensor and J is the Jacobian of the deformation gradient. The kinetic, strain, and total energy of the system are presented in Figure 17. It is evident that the proposed method yields a constant total energy throughout the simulation period as desired.

5.4. Stability analysis using pulling test of column

In this example we assess the numerical stability of the proposed TLSPH method using a three-dimensional column subjected to extreme elongation. The square column has a width of $w = 1$ m and has initial length of $L = 6$ m. The physical fields are discretised using $12 \times 12 \times 72$ uniformly distributed particles. Here we use a cubic b-spline kernel with first order correction and a width of $h = 0.5$. The column is made from rubber with elasticity modulus $E = 17$ MPa, $\nu = 0.45$, and $\rho = 1100$ kg/m³. The bottom end of the column is fixed and the free top end is subjected

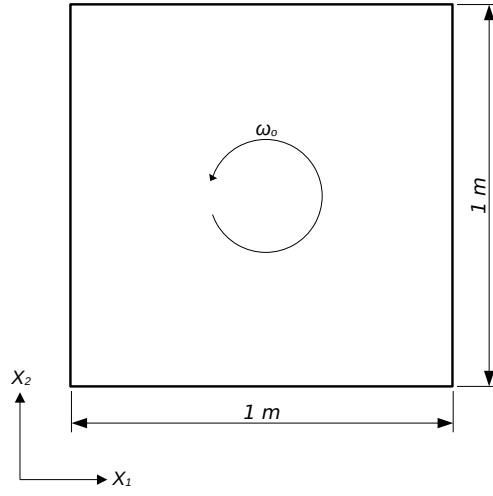


Figure 10: Configuration and dimension of the spinning plate

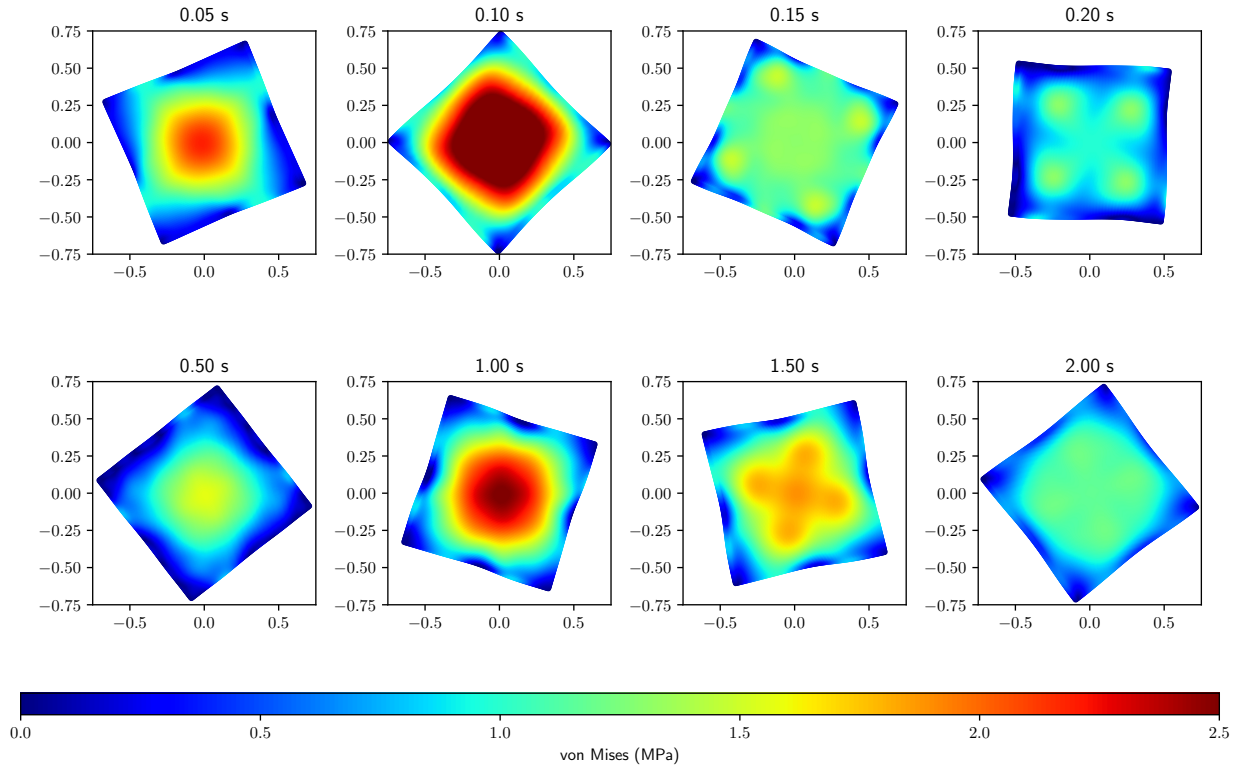


Figure 11: Stress contours of the spinning plate at various time frames

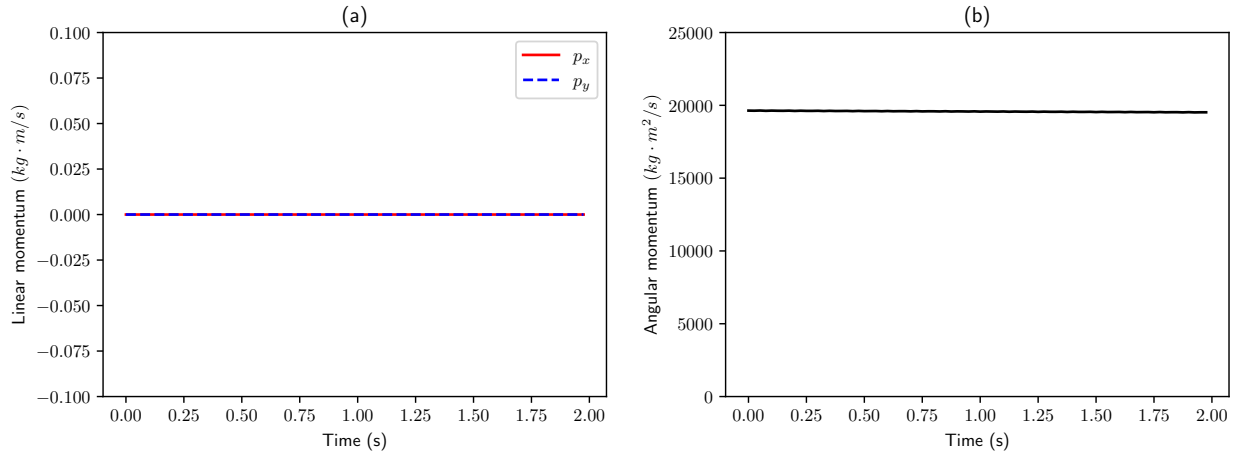


Figure 12: Momentum preservation of the spinning plate problem: (a) linear momentum, (b) angular momentum

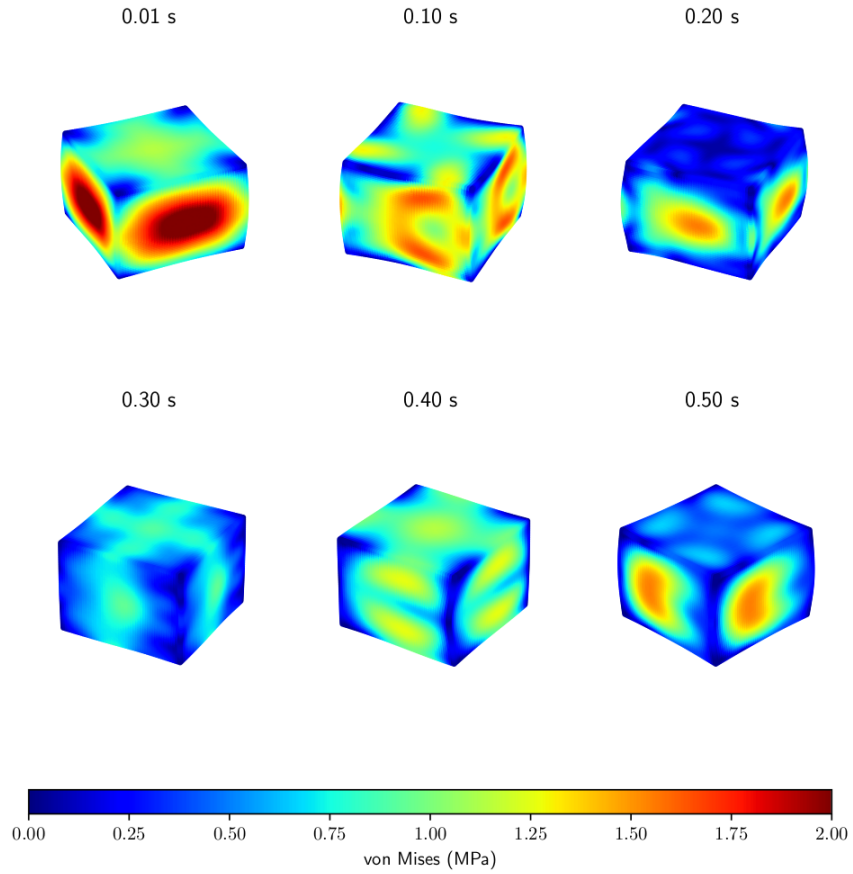


Figure 13: Stress contours of the spinning cube at various time frames

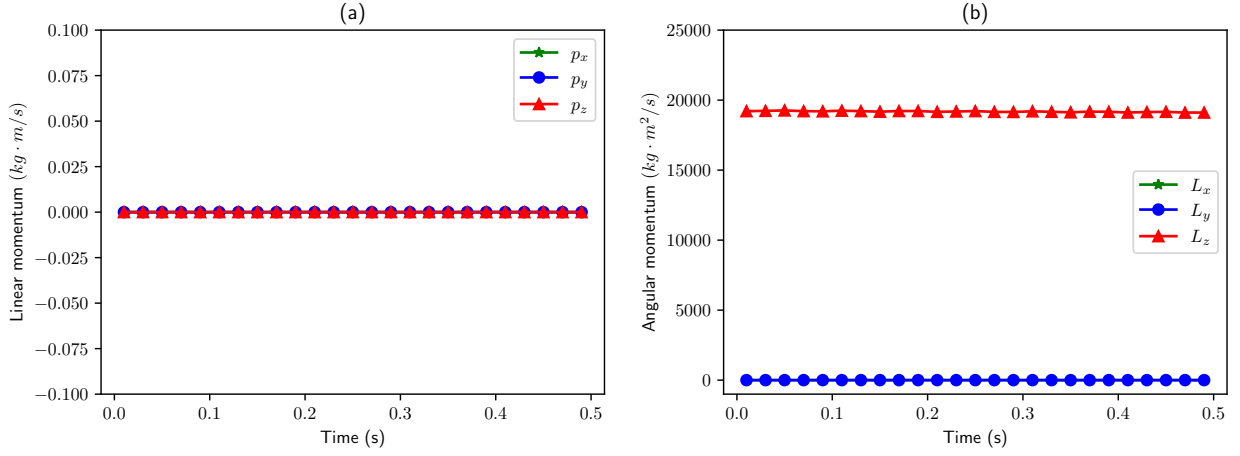


Figure 14: Momentum preservation of the spinning cube problem: (a) linear momentum, (b) angular momentum

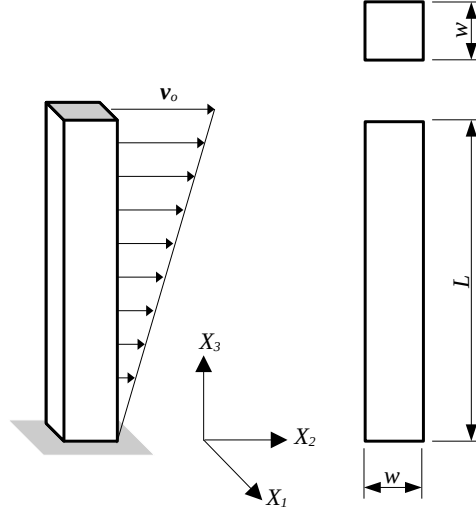


Figure 15: Configuration and dimension of the column for energy preservation analysis

to a constant velocity $\mathbf{v} = (0, 0, 10)$ m/s, as shown in Figure 18. We aim to continue the simulation until it fails to produce a stable result. The maximum stretch in X_3 direction λ_3 is calculated as follows

$$\lambda_3 = \frac{L' - L}{L} \times 100\% \quad (45)$$

where L' is the final length of the column. The JST parameters used in this example are $\eta^{(2)} = 0.5$ and $\eta^{(4)} = 0.6$.

We compare the maximum stretch of the column produced using the standard SPH discretisation and our proposed method with the improved bond-based deformation gradient formulation. The particle displacements and the respective von Mises stress are presented in Figure 19. In standard SPH, the instability occurs when $\lambda_3 = 257\%$, which is manifested through particle detachment and the "NaN" results in displacement and stress values. In contrast, simulations using SPH with the improved bond-based deformation gradient remain stable even at $\lambda_3 = 257\%$ and can continue until $\lambda_3 = 321\%$ before encountering instability. This means that the proposed method achieves a tensile strain approximately 25% higher than the standard SPH. Even at such extreme elongation, particle detachments are not as severe as the one shown using the standard SPH. These results highlight the stability improvement achieved by the proposed method, enabling it to handle large tensile strains.

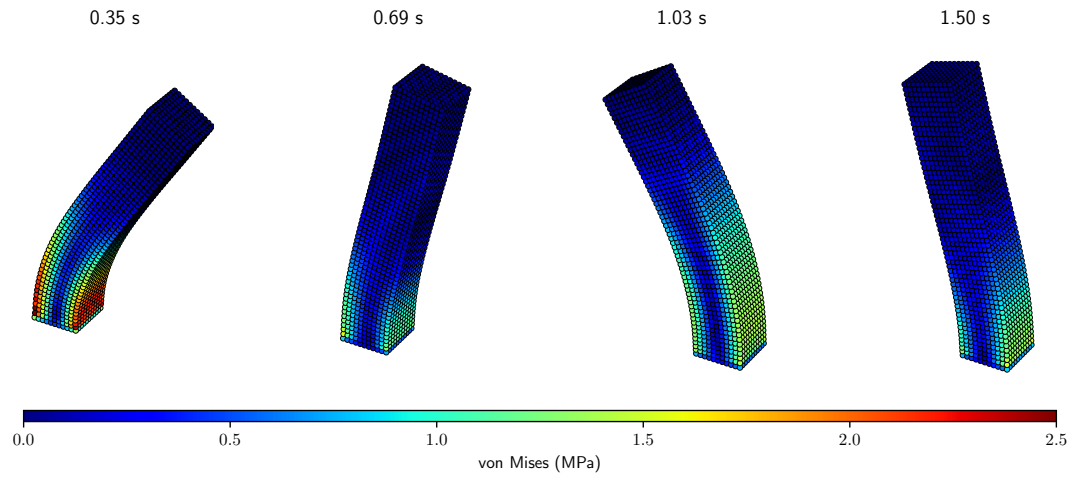


Figure 16: Deformation and stress distribution of the column at various time frames

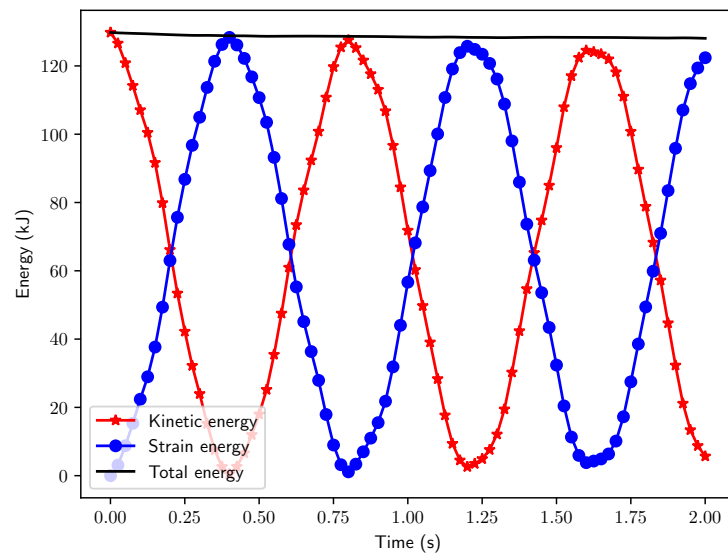


Figure 17: Energy preservation of the column for a long term response

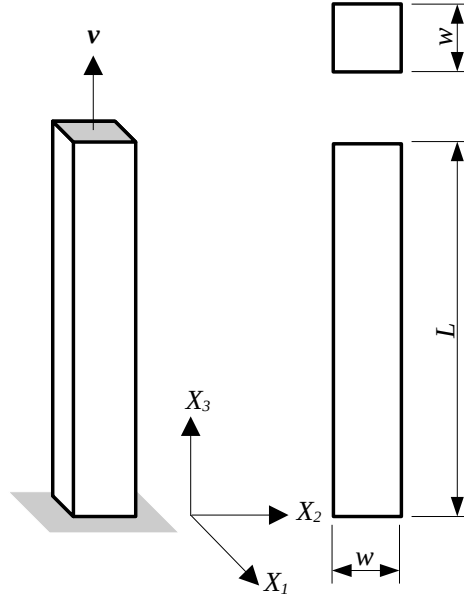


Figure 18: Configuration and dimension of the column for the pulling test

SPH - $\lambda_z = 257\%$

Proposed SPH - $\lambda_z = 257\%$

Proposed SPH - $\lambda_z = 321\%$

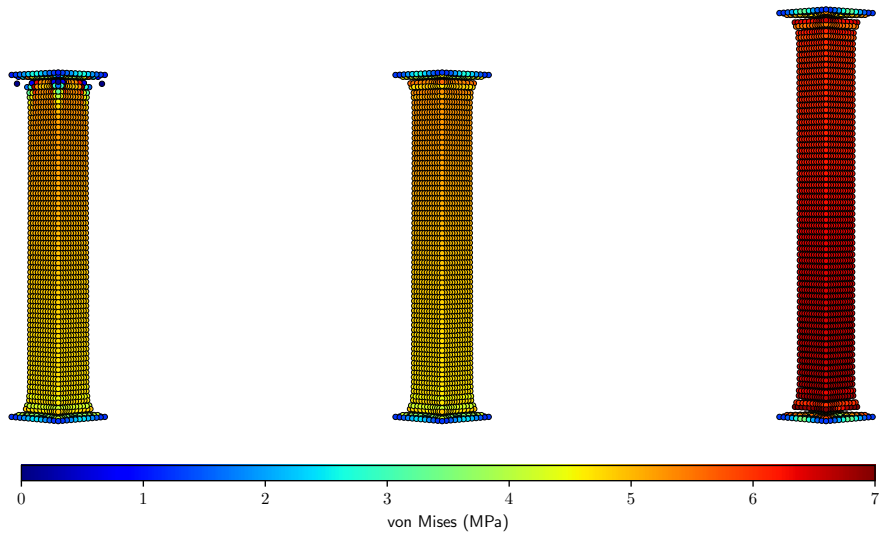


Figure 19: Deformation and stress contour of a column which pulled by a constant speed.

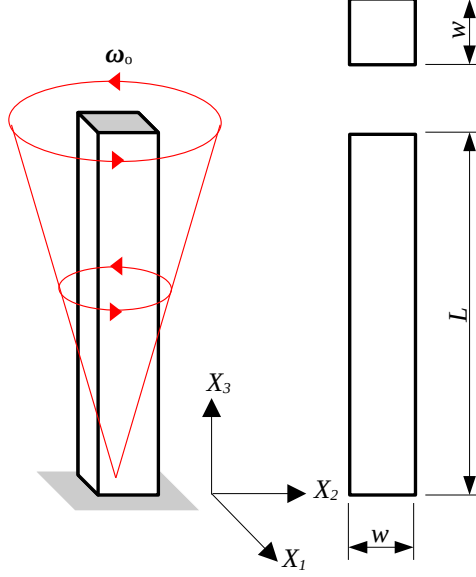


Figure 20: Configuration and dimension of the twisting column problem

5.5. Stability analysis using twisting column problem

Our final example involves the twisting of a three-dimensional column with extremely large deformation. The square column is $1 \times 1 \times 6$ m and is fixed at the bottom end, as depicted in Figure 20. An initial angular velocity $\omega_o = (0, 0, \omega_3 \sin(\pi X_3/12))^T$ is applied to the column at time $t = 0$ s. The deformation of the column and the von Mises stress for $\omega_3 = 105$ rad/s are presented in Figure 21 for various particle discretisations at time $t = 100$ ms. It is evident that our proposed method exhibits the expected deformation patterns for all discretisations, even with a sparse $4 \times 4 \times 24$ particles. This is already an improvement with respect to the original TLSPH with JST stabilisation [62], which requires a dense particle distribution to obtain a stable result with accurate deformation pattern. Our presented results are comparable with the upwind-SPH shown in [41].

Next we investigate the effect of time increment on the numerical stability of the proposed method through the variation of the CFL constant $\alpha_{CFL} \in \{0.1, 0.4, 0.9\}$. The results are presented in Figure 22 for $\omega_3 = 105$ m/s recorded at time $t = 100$ ms (upper row) and $t = 250$ ms (bottom row). The results agree well with those presented in [62]. The use of the three-stage time integrator allows for the use of higher α_{CFL} , leading to a lower computational cost. Additionally, the numerical stability and accuracy are well-maintained, as evidenced by the consistent deformed shape and stress distribution.

Lastly we investigate the effect of the initial angular velocity applied to the column, denoted as ω_3 . Figure 23 illustrates the deformed shape with $\omega_3 = 300$ rad/s. As reported in [57], solving this problem with the standard SPH leads to numerical instability and particle detachment. In contrast, the proposed formulation exhibits stable results until $t = 92.1$ ms. To create an even more interesting and challenging test, we further increase the angular velocity to $\omega_3 = 400$ rad/s. The results are shown in Figure 24. It is evident that the simulation remains stable even for extremely large deformation.

6. Conclusions

We presented a total Lagrangian Smoothed Particle Hydrodynamics (TLSPH) method designed for large-strain solid dynamics problems, showcasing optimal convergence and improved stability. Specifically, our approach involves a bond-based deformation gradient computed at particle pairs smoothed by a compactly supported Lagrangian kernel. Additionally, we consider the bond of a particle with itself to maintain the method's consistency established by the kernel correction. The concept was initially illustrated in one dimension and its excellent properties were demonstrated through the gradient estimation of polynomial and oscillatory deformation field. Intergration into the TLSPH

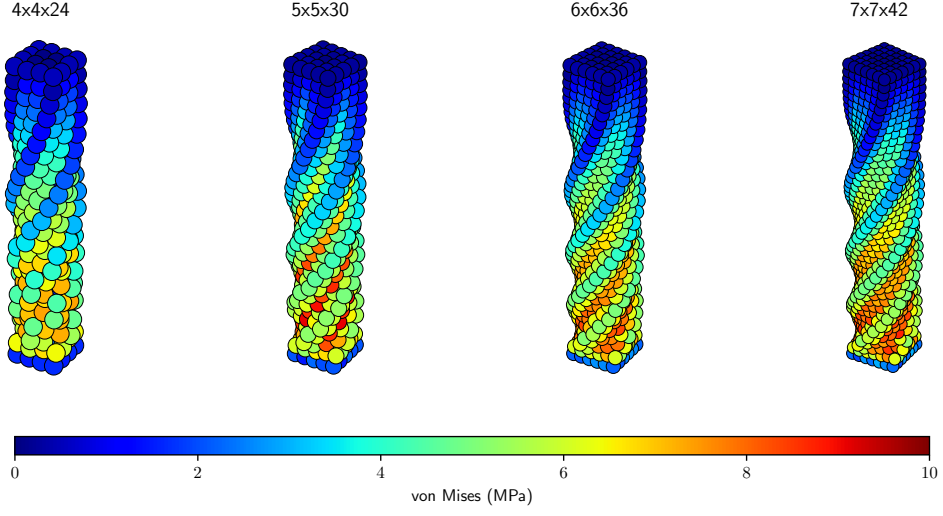


Figure 21: Analysis of particle refinement on the deformation of twisting column with $\omega_3 = 105 \text{ rad/s}$, $E = 17 \text{ MPa}$, $\nu = 0.45$, $\rho = 1100 \text{ kg/m}^3$, $\alpha_{CFL} = 0.9$, $\eta^{(2)} = 0$ and $\eta^{(4)} = 0.125$. The results were recorded at $t = 100 \text{ ms}$

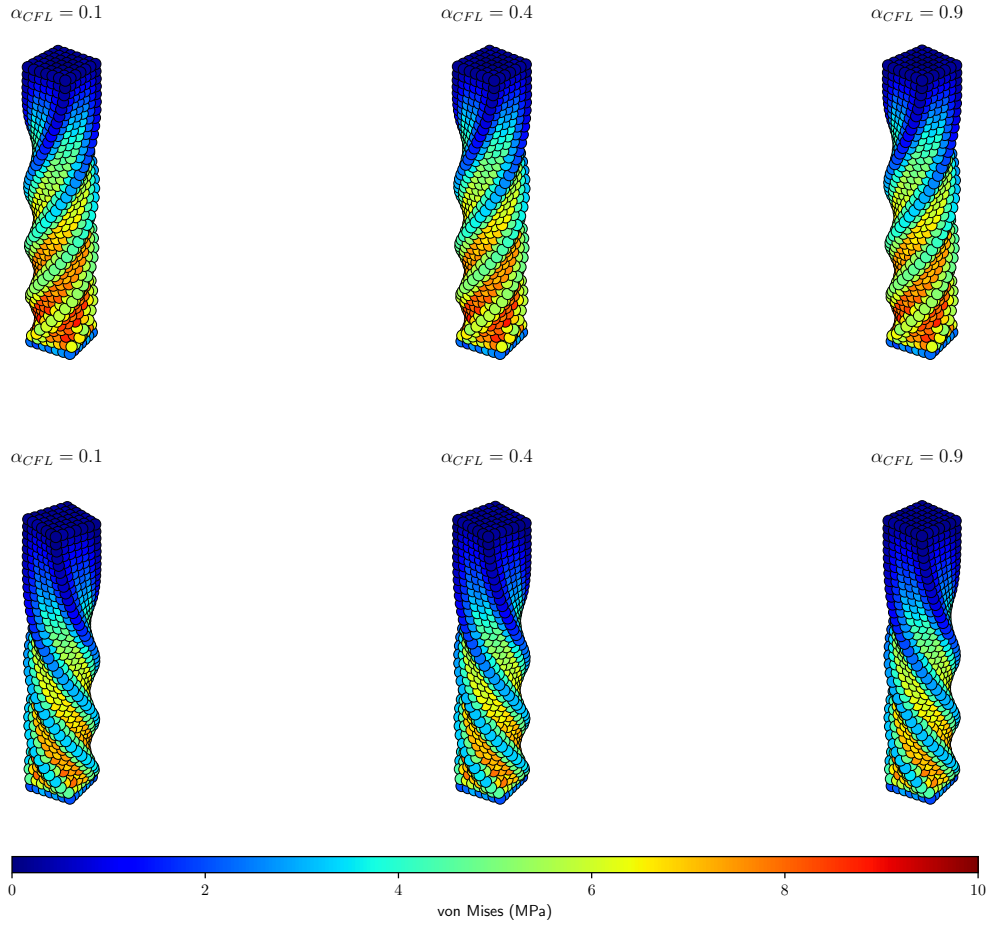


Figure 22: Analysis of time increment on the deformation of twisting column with particle configuration $7 \times 7 \times 42$, $\omega_3 = 105 \text{ rad/s}$, $E = 17 \text{ MPa}$, $\nu = 0.45$, $\rho = 1100 \text{ kg/m}^3$, $\eta^{(2)} = 0$ and $\eta^{(4)} = 0.125$. The upper row of the figure was recorded at $t = 100 \text{ ms}$, and the bottom row at $t = 250 \text{ ms}$

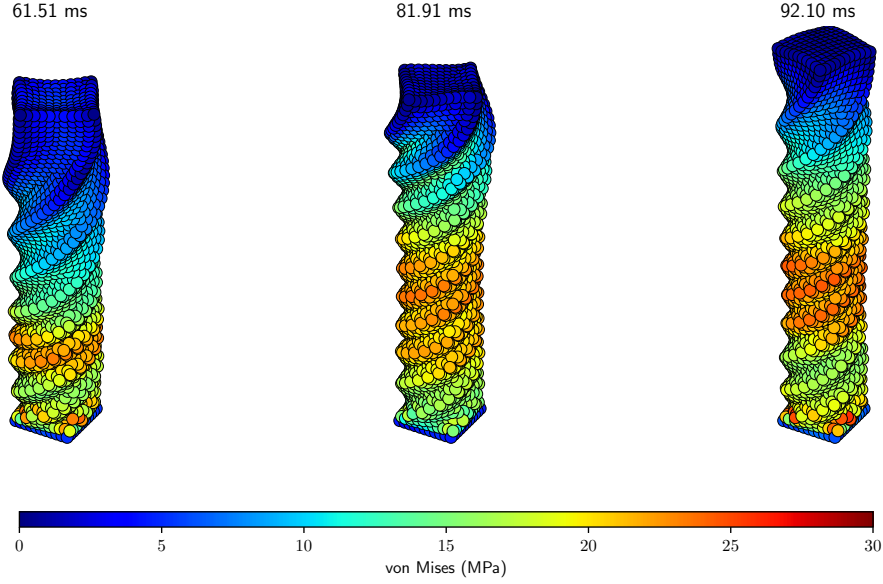


Figure 23: Deformation of twisting column with particle configuration $11 \times 11 \times 66$, $\omega_3 = 300 \text{ rad/s}$, $E = 17 \text{ MPa}$, $\nu = 0.49$, $\rho = 1100 \text{ kg/m}^3$, $\alpha_{CFL} = 0.5$, $\eta^{(2)} = 0$ and $\eta^{(4)} = 0.125$.

framework involved incorporating it as a correction to the standard, or averaged, deformation gradient. Our proposed framework retains optimal convergence rates in L_2 -norm and H_1 -seminorm of displacement, stemming from the first order kernel correction, which ensures linear polynomial reproducibility. We have also shown that the proposed method preserves linear and angular momentum, as well as the total energy throughout simulations. Furthermore, our deformation gradient formulation exhibits increased stability in cases involving large strain, as illustrated in our pulling and twisting of column examples. In the pulling case, a strain up to 25% larger can be achieved without spurious oscillations due to zero-energy modes, compared to TLSPH using the standard deformation gradient formulation. Notably, the proposed method requires the computation of the corrective bond-based gradient for each pair within the neighbourhood of a particle. However, due to its total Lagrangian construction, this computation can be efficiently performed without reidentifying the neighbours.

There are several promising future developments of the proposed method. The first concerns integrating the bond-based deformation gradient in the updated-Lagrangian SPH framework. This will enable computation of complex problems involving topological changes, such as crack propagation and free surface flow. Another promising direction follows the findings in our one-dimensional analysis, which indicates that the proposed improved bond-based deformation gradient is more accurate for higher order polynomial or highly oscillatory fields. This has potential applications in unsteady analyses of both solid and fluid dynamics.

Acknowledgments

The authors gratefully acknowledge the Penelitian Dasar administrated by Direktorat Riset dan Pengabdian Masyarakat - Direktorat Jenderal Penguatan Riset dan Pengembangan - Kementerian Riset dan Teknologi/Badan Riset dan Inovasi Nasional, Republik Indonesia, for the support funding of this research. The authors also thank Chun Hean Lee for the stimulating discussion on the topic.

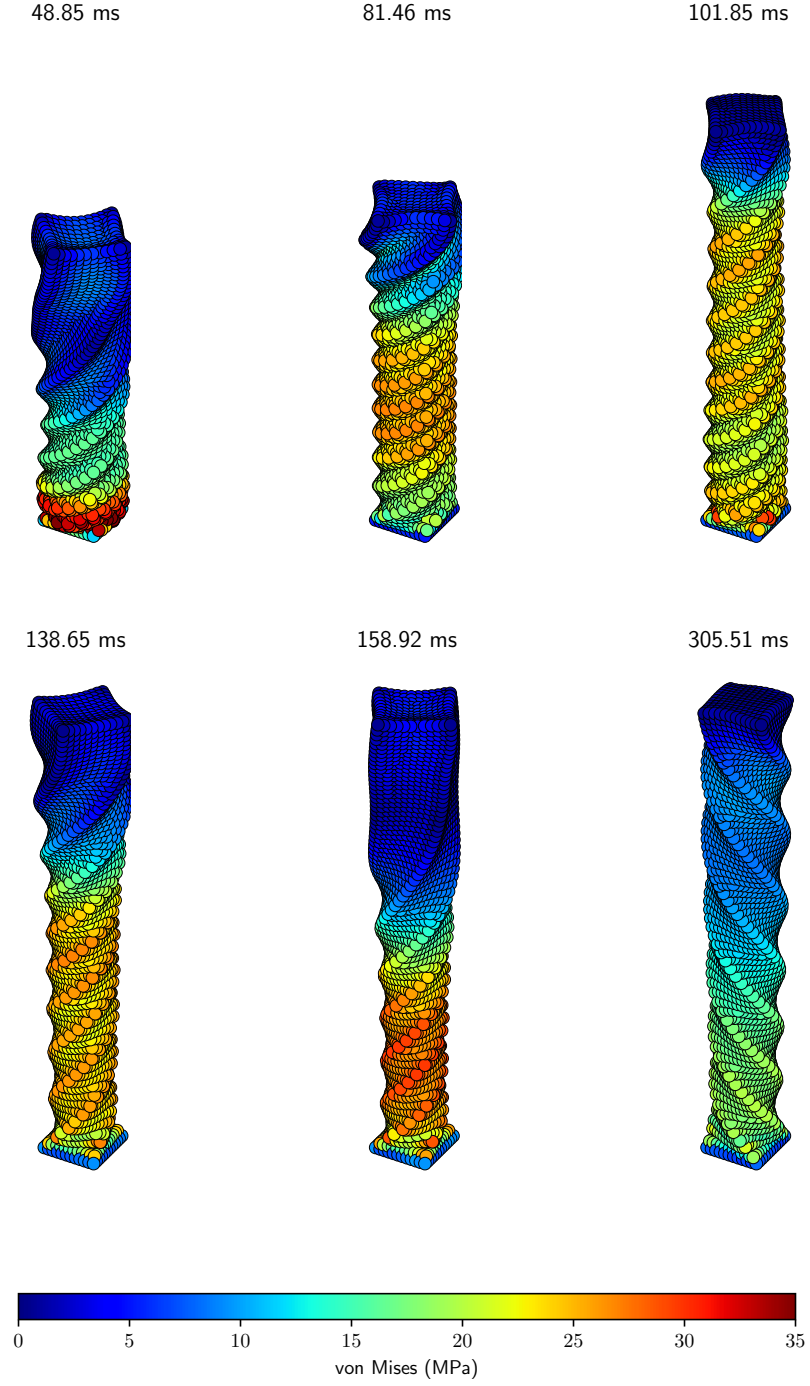


Figure 24: Deformation of twisting column with particle configuration $12 \times 12 \times 72$, $\omega_3 = 400 \text{ rad/s}$, $E = 17 \text{ MPa}$, $\nu = 0.49$, $\rho = 1100 \text{ kg/m}^3$, $\alpha_{CFL} = 0.5$, $\eta^{(2)} = 0$ and $\eta^{(4)} = 0.6$.

Appendix A. Gradient of the first order corrected kernel

In this appendix we present the derivation to obtain the gradient of the first order corrected kernel $\nabla \tilde{W}_i^1(\mathbf{x}_j)$ as previously described in Section 2.2. First we define a compact notation $\mathbf{x}_{ij} = \mathbf{x}_i - \mathbf{x}_j$ for the vector between two coordinates \mathbf{x}_i and \mathbf{x}_j . We then rewrite equation 6 as

$$\tilde{W}_i^1(\mathbf{x}_j) = \alpha_i (1 + \boldsymbol{\beta}_i \cdot \mathbf{x}_{ij}) W_i(\mathbf{x}_j). \quad (\text{A.1})$$

The coefficients α_i and $\boldsymbol{\beta}_i$ in (A.1) are described as

$$\alpha_i = \left(\varphi_i - \left((\boldsymbol{\Phi}_i)^{-1} \boldsymbol{\phi}_i \right) \cdot \boldsymbol{\phi}_i \right)^{-1}, \quad (\text{A.2a})$$

$$\boldsymbol{\beta}_i = -(\boldsymbol{\Phi}_i)^{-1} \boldsymbol{\phi}_i. \quad (\text{A.2b})$$

where φ_i , $\boldsymbol{\phi}_i$, and $\boldsymbol{\Phi}_i$ are the geometric moments of the kernel centred at \mathbf{x}_i , which are given by

$$\varphi_i = \sum_{j \in \mathcal{N}(\mathbf{x}_i)} V_j W_i(\mathbf{x}_j), \quad (\text{A.3a})$$

$$\boldsymbol{\phi}_i = \sum_{j \in \mathcal{N}(\mathbf{x}_i)} \mathbf{x}_{ij} V_j W_i(\mathbf{x}_j), \quad (\text{A.3b})$$

$$\boldsymbol{\Phi}_i = \sum_{j \in \mathcal{N}(\mathbf{x}_i)} \mathbf{x}_{ij} \otimes \mathbf{x}_{ij} V_j W_i(\mathbf{x}_j). \quad (\text{A.3c})$$

The gradient of the first order corrected kernel $\nabla \tilde{W}_i^1(\mathbf{x}_j)$ can be obtained by differentiating A.1, which yields

$$\nabla \tilde{W}_i^1(\mathbf{x}_j) = \alpha_i (1 + \boldsymbol{\beta}_i \cdot \mathbf{x}_{ij}) \nabla W_i(\mathbf{x}_j) + \nabla \alpha_i (1 + \boldsymbol{\beta}_i \cdot \mathbf{x}_{ij}) W_i(\mathbf{x}_j) + \alpha_i \left((\nabla \boldsymbol{\beta}_i)^\top \cdot \mathbf{x}_{ij} + \boldsymbol{\beta}_i \right) W_i(\mathbf{x}_j). \quad (\text{A.4})$$

The derivative of α_i and $\boldsymbol{\beta}_i$ with respect to coordinate axis k are given as

$$\nabla_k \alpha_i = -\alpha_i^2 \left(\nabla_k \varphi_i - \left((\boldsymbol{\Phi}_i)^{-1} \boldsymbol{\phi}_i \right) \cdot \nabla_k \boldsymbol{\phi}_i - \left((\boldsymbol{\Phi}_i)^{-1} \nabla_k \boldsymbol{\phi}_i \right) \cdot \boldsymbol{\phi}_i + \left((\boldsymbol{\Phi}_i)^{-1} \nabla_k \boldsymbol{\Phi}_i (\boldsymbol{\Phi}_i)^{-1} \boldsymbol{\phi}_i \right) \cdot \boldsymbol{\phi}_i \right), \quad (\text{A.5a})$$

$$\nabla_k \boldsymbol{\beta}_i = -(\boldsymbol{\Phi}_i)^{-1} \nabla_k \boldsymbol{\phi}_i + (\boldsymbol{\Phi}_i)^{-1} \nabla_k \boldsymbol{\Phi}_i (\boldsymbol{\Phi}_i)^{-1} \boldsymbol{\phi}_i. \quad (\text{A.5b})$$

In the above, the derivate of the geometric moments are given as follows

$$\nabla \varphi_i = \sum_{j \in \mathcal{N}(\mathbf{x}_i)} V_j \nabla W_i(\mathbf{x}_j) \quad (\text{A.6a})$$

$$\nabla \boldsymbol{\phi}_i = \sum_{j \in \mathcal{N}(\mathbf{x}_i)} V_j \left(\mathbf{x}_{ij} \otimes \nabla W_i(\mathbf{x}_j) + \mathbf{I} W_i(\mathbf{x}_j) \right) \quad (\text{A.6b})$$

$$\nabla_k \boldsymbol{\Phi}_i = \sum_{j \in \mathcal{N}(\mathbf{x}_i)} V_j \left(\mathbf{x}_{ij} \otimes \mathbf{x}_{ij} \nabla_k W_i(\mathbf{x}_j) + \left(\mathbf{x}_{ij} \otimes \boldsymbol{\delta}^k + \boldsymbol{\delta}^k \otimes \mathbf{x}_{ij} \right) W_i(\mathbf{x}_j) \right), \quad (\text{A.6c})$$

where \mathbf{I} and $\boldsymbol{\delta}^k$ denote an identity matrix and a unit vector in the k -th direction, respectively. Note that although an explicit formulation can be obtained, the computation of the first derivative $\nabla \tilde{W}_i^1(\mathbf{x}_j)$ is more involved. This includes obtaining the tensor $\nabla_k \boldsymbol{\Phi}_i$ and a small matrix inversion $(\boldsymbol{\Phi}_i)^{-1}$ for each position \mathbf{x}_i .

References

- [1] L. Lucy, A numerical approach to the testing of the fission hypothesis, *The Astronomical Journal* 82 (1977) 1013–1024.
- [2] R. Gingold, J. Monaghan, Smoothed particle hydrodynamics: theory and application to non-spherical stars, *Royal Astronomical Society* 181 (1977) 375–389.
- [3] Y. Vidal, J. Bonet, A. Huerta, Stabilized updated lagrangian corrected sph for explicit dynamic problems, *Int. J. Numer. Meth. Engng* 69 (2007) 2687–2710.
- [4] T. J. R. Hughes, J. A. Cottrell, Y. Bazilevs, Isogeometric analysis: CAD, finite elements, NURBS, exact geometry and mesh refinement, *Computer Methods in Applied Mechanics and Engineering* 194 (2005) 4135–4195.
- [5] M. Liu, G. Liu, Smoothed particle hydrodynamics (sph): an overview and recent developments, *Arch. Comput. Methods. Eng.* 17 (2010) 25–76.
- [6] L. Libersky, A. Petschek, T. Carney, J. Hipp, F. Allahdadi, High strain lagrangian hydrodynamics: A three-dimensional sph code for dynamic material response, *Journal of Computational Physics* 109 (1993) 67–75.
- [7] J. Chen, J. Beraun, A generalized smoothed particle hydrodynamics method for nonlinear dynamic problems, *Computational Methods in Applied Mechanics and Engineering* 190 (2000) 225–239.
- [8] K. Ganesh, M. Islam, P. Patra, K. Travis, Multi-scale modelling of fatigue crack propagation due to liquid droplet impingement, *Proc. R. Soc. A.* 479 (2022) 0380.
- [9] K. Ganesh, M. Islam, P. Patra, K. Travis, A pseudo-spring based sph framework for studying fatigue crack propagation, *International Journal of Fatigue* 162 (2022) 106986.
- [10] R. Stellingwerf, C. Wingate, Impact modelling with smooth particle hydrodynamics, *International Journal of Impact Engineering* 14 (1993) 707–718.
- [11] G. Johnson, R. Stryk, S. Beissel, Sph for high velocity impact computations, *Computational Methods in Applied Mechanics and Engineering* 139 (1996) 347–373.
- [12] S. Chakraborty, A. Shaw, A pseudo-spring based fracture model for sph simulation of impact dynamics, *International Journal of Impact Engineering* 58 (2013) 84–95.
- [13] M. Islam, S. Chakraborty, A. Shaw, S. Reid, A computational model for failure of ductile material under impact, *International Journal of Impact Engineering* 108 (2017) 334–347.
- [14] R. Vignjevic, J. Campbell, Review of development of the smooth particle hydrodynamics (sph) method, *Predictive Modeling of Dynamic Processes* (2009) 367–369.
- [15] R. Vacondio, C. Altomare, D. T. M.D. Leffe, X. Hu, J. M. S. Lind, S. Marrone, B. Rogers, A. Iglesias, Grand challenges for smoothed particle hydrodynamics numerical schemes, *Computational Particle Mechanics* 8 (2021) 575–588.
- [16] J. Bonet, S. Kulasegaram, Correction and stabilization of smooth particle hydrodynamics methods with applications in metal forming simulations, *Int. J. Numer. Methods Eng.* 47 (2000) 1189–1214.
- [17] N. Frontiere, C. D. Raskin, J. M. Owen, Crksph – a conservative reproducing kernel smoothed particle hydrodynamics scheme, *Journal of Computational Physics* 332 (2017) 160–209.
- [18] W. K. Liu, S. Jun, Y. F. Zhang, Reproducing kernel particle methods, *International Journal for Numerical Methods in Fluids* 20 (1995) 1081–1106.
- [19] J. Bonet, T. Lok, Variational and momentum preservation aspects of smooth particle hydrodynamic formulations, *Computational Methods in Applied Mechanics and Engineering* 180 (1999) 97–115.
- [20] M. Liu, G. Liu, Restoring particle consistency in smoothed particle hydrodynamics, *Applied Numerical Mathematics* 56 (2006) 19–36.
- [21] M. Islam, S. Chakraborty, Shaw, On consistency and energy conservation in smoothed particle hydrodynamics, *International Journal for Numerical Methods in Engineering* 116(9) (2018) 601–632.
- [22] J. Swegle, D. Hicks, S. Attaway, Smoothed particle hydrodynamics stability analysis, *Journal of Computational Physics* 116 (1995) 123–134.
- [23] T. Belytschko, Y. Guo, W. Kam Liu, S. Ping Xiao, A unified stability analysis of meshless particle methods, *International Journal for Numerical Methods in Engineering* 48 (2000) 1359–1400.
- [24] J. Monaghan, Simulating free surface flows with sph, *Journal of Computational Physics* 110 (1994) 399–406.
- [25] J. Owen, A tensor artificial viscosity for sph, *Journal of Computational Physics* 201 (2004) 601–629.
- [26] J. Monaghan, Sph without a tensile instability, *Journal of Computational Physics* 159 (2000) 290–311.
- [27] P. Randles, L. Libersky, Smoothed particle hydrodynamics: Some recent improvements and applications, *Computational Methods in Applied Mechanics and Engineering* 139 (1996) 375–408.
- [28] D. Hicks, J. Swegle, S. Attaway, Conservative smoothing stabilizes discrete-numerical instabilities in sph material dynamics computations, *Applied Mathematics and Computation* 85 (1997) 209–226.
- [29] D. Hicks, L. Liebrock, Conservative smoothing with b-splines stabilizes sph material dynamics in both tension and compression, *Applied Mathematics and Computation* 150 (213-234) 2004.
- [30] C. Guenther, D. Hicks, J. Swegle, Conservative smoothing versus artificial viscosity, *Tech. Rep. Sandia National Labs.* (1994).
- [31] S. Lahiri, K. Bhattacharya, A. Shaw, L. Ramachandra, A stable sph with adaptive b-spline kernel, *Journal of Computational Physics* 422 (2020) 109761.
- [32] C. Dyka, P. Randles, R. Ingel, Stress points for tension instability in sph, *Int. J. Numer. Methods Eng.* 40 (1997) 2325–2341.
- [33] L. Wang, F. Xu, Y. Yang, Improvement of the tensile instability in sph scheme for the fei (fluid-elastomer interaction) problem, *Engineering Analysis with Boundary Elements* 106 (2019) 116–125.
- [34] J. Bonet, S. Kulasegaram, Remarks on tension instability of eulerian and lagrangian corrected smooth particle hydrodynamics (csph) methods, *International Journal for Numerical Methods in Engineering* 52 (2001) 1203–1220.
- [35] T. Rabczuk, T. Belytschko, S. Xiao, Stable particle methods based on lagrangian kernels, *Comput. Methods Appl. Mech. Engrg.* 193 (193) 1035–1063.
- [36] R. Vignjevic, J. Reves, J. Campbell, Sph in a total lagrangian formalism, *Tech Science Press* 14(3) (2006) 181–198.

- [37] J. Lin, H. Naceur, D. Coutellier, A. Laksimi, Efficient meshless sph method for the numerical modeling of thick shell structures undergoing large deformations, *International Journal of Non-Linear Mechanics* 65 (2014) 1–13.
- [38] J. Lin, H. Naceur, D. Coutellier, A. Laksimi, Geometrically nonlinear analysis of thin-walled structures using efficient shell-based sph method, *Computational Materials Science* 85 (2014) 127–133.
- [39] J. Lin, J. Li, Y. Guan, G. Zhao, H. Naceur, D. Coutellier, Geometrically nonlinear bending analysis of functionally graded beam with variable thickness by a meshless method, *Composite Structures* 189 (2018) 239–246.
- [40] C. Lee, A. Gill, O. Hassan, J. Bonet, S. Kulasegaram, A variationally consistent streamline upwind petrov–galerkin smooth particle hydrodynamics algorithm for large strain solid dynamics, *Comput. Methods Appl. Mech. Engrg.* 318 (2017) 514–536.
- [41] C. Lee, A. Gill, A. Ghavamian, J. Bonet, A total lagrangian upwind smooth particle hydrodynamics algorithm for large strain explicit solid dynamics, *Comput. Methods Appl. Mech. Engrg.* 344 (2019) 209–250.
- [42] I. Wiragunarsa, L. Zuhail, T. Dirgantara, I. Putra, A particle interaction-based crack model using an improved smoothed particle hydrodynamics for fatigue crack growth simulation, *Int. J. Fract.* 229 (2021) 229–244.
- [43] D. Flanagan, T. Belytschko, A uniform strain hexahedron and quadrilateral with orthogonal hourglass control, *International Journal for Numerical Methods in Engineering* 17 (1981) 679–706.
- [44] O. Jaquod, J. Oden, Analysis of hourglass instabilities and control in underintegrated finite element methods, *Comput. Methods Appl. Mech. Engrg.* 44 (1984) 339–363.
- [45] M. Antuono, A. Colagrossi, S. Marrone, D. Molteni, Free-surface flows solved by means of sph schemes with numerical diffusive terms, *Computer Physics Communications* 181 (2010) 532–549.
- [46] M. Antuono, A. Colagrossi, S. Marrone, Numerical diffusive terms in weakly-compressible sph schemes, *Computer Physics Communications* 183 (2012) 2570–2580.
- [47] I. Hammani, S. Marrone, A. Colagrossi, G. Oger, D. Touze, Detailed study on the extension of the δ -sph model to multi-phase flow, *Comput. Methods Appl. Mech. Engrg.* 368 (2020) 113189.
- [48] Z. Meng, A. Zhang, J. Yan, P. Wang, A. Khayyer, A hydroelastic fluid–structure interaction solver based on the riemann-sph method, *Comput. Methods Appl. Mech. Engrg.* 390 (2022) 114522.
- [49] C. T. Nguyen, C. T. Nguyen, H. Bui, G. Nguyen, R. Fukagawa, A new sph-based approach to simulation of granular flows using viscous damping and stress regularisation, *Landslides* 14 (2017) 69–81.
- [50] Y. Lian, H. Bui, G. Nguyen, A. Haque, An effective and stabilised ($\mathbf{u}-p_I$) sph framework for large deformation and failure analysis of saturated porous media, *Comput. Methods Appl. Mech. Engrg.* 408 (2023) 115967.
- [51] R. Vignjevic, J. Campbell, L. Libersky, A treatment of zero-energy modes in the smoothed particle hydrodynamics method, *Computer Methods in Applied Mechanics and Engineering* 184 (2000) 67–85.
- [52] P. Randles, L. Libersky, Normalized sph with stress points, *Int. J. Numer. Methods Eng.* 48 (2000) 1445–1462.
- [53] S. Armfield, Finite difference solutions of the navier-stokes equations on staggered and non-staggered grids, *Computers Fluids* 20 (1991) 1–17.
- [54] B. Hustedt, S. Operto, J. Virieux, Mixed-grid and staggered-grid finite-difference methods for frequency-domain acoustic wave modelling, *Geophys. J. Int.* 157 (2004) 1269–1296.
- [55] Y. Liu, M. Sen, An implicit staggered-grid finite-difference method for seismic modelling, *Geophys. J. Int.* 179 (2009) 459–474.
- [56] G. Ganzenmuller, An hourglass control algorithm for lagrangian smooth particle hydrodynamics, *Comput. Methods Appl. Mech. Engrg.* 286 (2015) 87–106.
- [57] D. Wu, C. Zhang, X. Tang, X. Hu, An essentially non-hourglass formulation for total lagrangian smoothed particle hydrodynamics, *Comput. Methods Appl. Mech. Engrg.* 407 (2023) 115915.
- [58] S. Silling, Stability of peridynamic correspondence material models and their particle discretizations, *Computer Methods in Applied Mechanics and Engineering* 322 (2017) 42–57.
- [59] T. Breitman, K. Dayal, Bond-level deformation gradients and energy averaging in peridynamics, *Journal of the Mechanics and Physics of Solids* 110 (2018) 192–204.
- [60] J. Bonet, A. Gil, C. Lee, M. Aguirre, R. Ortigosa, A first order hyperbolic framework for large strain computational solid dynamics - part i: Total lagrangian isothermal elasticity, *Comput. Methods Appl. Mech. Engrg.* 283 (2015) 689–732.
- [61] M. Aguirre, A. Gil, J. Bonet, A. A.C., A vertex centered finite volume jameson-schmidt-turkel (jst) algorithm for a mixed conservation formulation in solid dynamics, *Journal of Computational Physics* 259 (2014) 672–699.
- [62] C. Lee, A. Gill, G. Greto, S. Kulasegaram, J. Bonet, A new jameson–schmidt–turkel smooth particle hydrodynamics algorithm for large strain explicit fast dynamics, *Comput. Methods Appl. Mech. Engrg.* 311 (2016) 71–111.
- [63] P. de Campos, A. Gill, C. Lee, M. Giacomini, J. Bonet, A new updated reference lagrangian smooth particle hydrodynamics algorithm for isothermal elasticity and elasto-plasticity, *Comput. Methods Appl. Mech. Engrg.* 392 (2022) 114680.
- [64] A. Jameson, Origins and further development of the jameson–schmidt–turkel scheme, *AIAA Journal* 55(5) (2017).
- [65] W. K. Liu, S. Jun, Y. F. Zhang, Reproducing kernel particle methods, *International Journal for Numerical Methods in Fluids* 20 (1995) 1081–1106.
- [66] C. Lee, A. Gill, J. Bonet, Development of a cell centred upwind finite volume algorithm for a new conservation law formulation in structural dynamics, *Computers and Structures* 118 (2013) 13–38.
- [67] M. Tupek, R. Radovitzky, An extended constitutive correspondence formulation of peridynamics based on nonlinear bond-strain measures, *Journal of the Mechanics and Physics of Solids* 65 (2014) 82–92.
- [68] K. Park, G. P. H. Chi, Numerical recipes for elastodynamic virtual element methods with explicit time integration, *Int J Numer Methods Eng.* 121 (2020) 1–31.
- [69] C. Lee, A. Gill, J. Bonet, Development of a stabilised petrov–galerkin formulation for conservation laws in lagrangian fast solid dynamics, *Comput. Methods Appl. Mech. Engrg.* 268 (2014) 40–64.